PHILOSOPHICAL TRANSACTIONS A

royalsocietypublishing.org/rsta

CC BY

Research

Cite this article: Herbst K, Dalla S, Engelbrecht NE, Muscheler R, Owens M, Zheng M. 2026 Assessing uncertainties in the numerical modelling of cosmogenic radionuclide production. *Phil. Trans. R. Soc. A* **384**: 20250348.
https://doi.org/10.1098/rsta.2025.0348

Received: 31 March 2026
Accepted: 30 June 2026

One contribution of 17 to a Theo Murphy meeting issue 'Radiocarbon and cosmic radiation events'.

Subject Areas:
astrophysics, solar system, atmospheric science

Keywords:
cosmic rays, modulation, cosmogenic radionuclides

Author for correspondence:
Konstantin Herbst
e-mail: konstantin.herbst@geo.uio.no

Supplementary material is available online at https://doi.org/10.6084/m9.figshare.c.8623422.

THE ROYAL SOCIETY PUBLISHING

Assessing uncertainties in the numerical modelling of cosmogenic radionuclide production

Konstantin Herbst[1], Silvia Dalla[2], N. Eugene Engelbrecht[3], Raimund Muscheler[4], Mathew Owens[5] and Minjie Zheng[6]

[1]Centre for Planetary Habitability (PHAB), Department of Geosciences, University of Oslo, Oslo, Norway
[2]Jeremiah Horrocks Institute, University of Lancashire, Preston, UK
[3]Centre for Space Research, Natural and Agricultural Sciences, North-West University, Potchefstroom, South Africa
[4]Department of Earth and Environmental Sciences (MGeo), Lund University, Lund, Sweden
[5]Department of Meteorology, University of Reading, Reading, Berkshire, UK
[6]School of Geographical Sciences, Fujian Normal University, Fuzhou, People's Republic of China

KH, 0000-0001-5622-4829; SD, 0000-0002-7837-5780; NEE, 0000-0003-3659-7956; RM, 0000-0003-2772-3631; MO, 0000-0003-2061-2453; MZ, 0000-0003-2111-9476

The terrestrial production of cosmogenic radionuclides such as ^{10}Be, ^{14}C and ^{36}Cl is triggered by spallation reactions of high-energy particles with atmospheric constituents such as oxygen, nitrogen and argon. After being produced and transported within the atmosphere, these radionuclides are deposited in natural archives, storing, for example, solar information over thousands of years. Therefore, records of ^{10}Be, ^{14}C and ^{36}Cl can be used to reconstruct solar activity back in time. However, to understand the underlying physical processes that dominate production and interpret the observations, numerical modelling is crucial. Here, we shall discuss the dependencies of the numerically derived production rates on a variety of factors that include the effects of the choice of the local interstellar spectrum (LIS), the geomagnetic field

© 2026 The Authors. Published by the Royal Society under the terms of the Creative Commons Attribution License http://creativecommons.org/licenses/by/4.0/, which permits unrestricted use, provided the original author and source are credited.

Downloaded from royalsocietypublishing.org/rsta/article-pdf/doi/10.1098/rsta.2025.0348/6165301/rsta.2025.0348.pdf
by guest
on 14 September 2026

and the production cross-sections available in the literature. We show that the investigated factors have modest to significant impacts on the modelled production rates of cosmogenic radionuclides and identify the discrepancies in the available cross-sections as the most crucial factor.

This article is part of the Theo Murphy meeting issue 'Radiocarbon and cosmic radiation events'.

1. Introduction

Energetic particles entering the Earth's atmosphere interact with atmospheric constituents such as nitrogen and oxygen. These interactions trigger the formation of secondary particle cascades and, consequently, the evolution of hadronic, muonic and electromagnetic branches. Since the discovery of these atmospheric particle showers in the early 1930s, scientists have conjectured that high-energy particles could generate cosmogenic radionuclides in the Earth's atmosphere [1]. This prediction was verified in the late 1940s with the discovery of ^{14}C [2,3]. However, the detection of other cosmogenic radionuclides required more advanced measurement techniques. It was the development of accelerator mass spectrometry (AMS, [4]) that provided a major breakthrough in the late 1970s and enabled the detection of additional isotopes such as ^{10}Be and ^{36}Cl. In fact, it is the hadronic branch, which consists primarily of protons and neutrons, that triggers the production of these three cosmogenic radionuclides.

Once produced in the atmosphere, the radionuclides are subsequently stored in natural archives, including ice sheets, tree rings and sediments [5]. As their production is influenced by the external impact of cosmic rays (CRs), which are modulated by solar activity, cosmogenic radionuclides have become essential tools for investigating past solar activity, CR variability and various processes within the Earth system. However, while these archives can now be analysed at high resolution, the resulting concentration records represent a complex interplay of production, transport and deposition. Therefore, a thorough interpretation of the radionuclide data necessitates the use of physically based production models that account for regional variability and can be integrated with atmospheric transport models.

The main drivers of radionuclide production are primary galactic CRs (GCRs) that are accelerated by supernova explosions and supernova remnants [6] and consist of approximately 87% protons, approximately 12% alpha particles and approximately 1% heavier particles [7]. Specifically, the low-energy part of the GCR distribution is modulated by being scattered at irregularities in the heliospheric magnetic field (HMF). The large-scale HMF further fosters GCRs to experience gradient and curvature drifts, while they further undergo convection and adiabatic deceleration in the expanding solar wind. Thus, there is a direct link between the omnidirectional GCR flux at Earth and the solar activity cycle.

However, in the past decade unexpected peak-like increases were observed in the ^{14}C, ^{10}Be and ^{36}Cl records around, for example, AD 774/775 and AD 992/993 [8–10], which triggered a debate about possible underlying causes. With a multi-radionuclide approach of highly resolved ^{10}Be records combined with ^{36}Cl ice core data, Mekhaldi *et al.* [10] could infer that extreme solar energetic particle (SEP) events, energetic particles accelerated in reconnection processes during solar flares and at the shock fronts of accompanying coronal mass ejections (CMEs), were the most likely causes behind these observations. Since then, it has been argued that not only GCRs but also SEPs play a crucial role in the production of cosmogenic radionuclides.

To gain a comprehensive understanding of the underlying physical processes, the production of cosmogenic radionuclides must be studied through numerical simulations. This requires a quantitative understanding of the modulation of GCRs by the HMF, the propagation of primary particles within the geomagnetic field, their interactions in the Earth's atmosphere and processing by the climate system. This necessitates a holistic approach that bridges knowledge of astrophysics, heliophysics and planetary sciences. While numerical schemes exist for all components of the system, many are based on overly simplistic approximations that introduce substantial—but as yet unquantified—uncertainties into estimates of the driving solar and cosmic energetic

Downloaded from royalsocietypublishing.org/rsta/article-pdf/doi/10.1098/rsta.2025.0348/6165301/rsta.2025.0348.pdf
by guest
on 14 September 2026

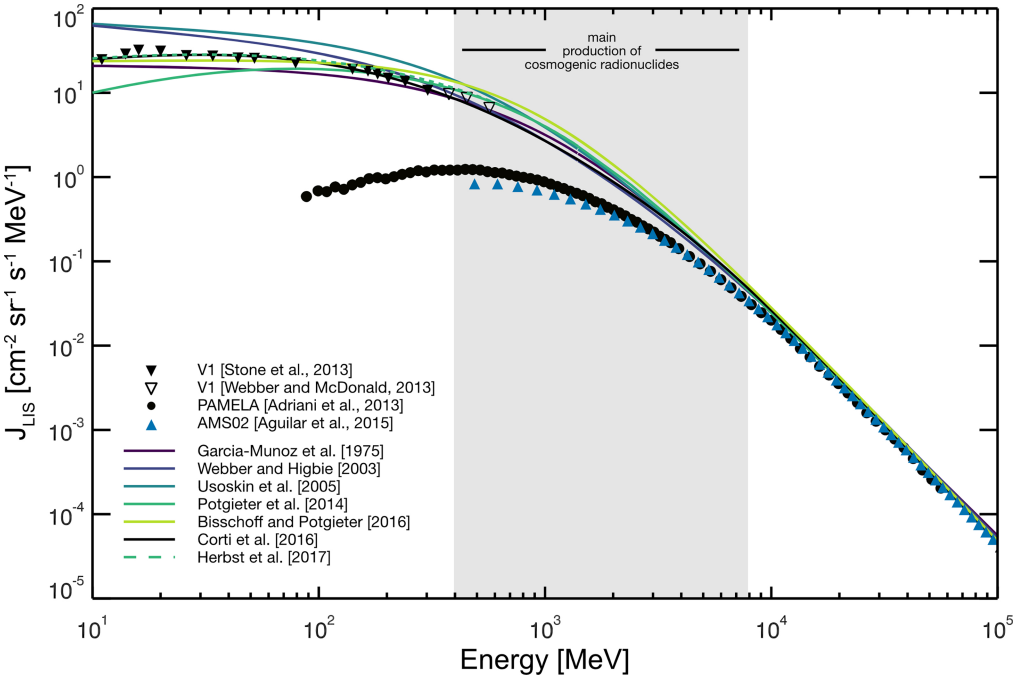


Figure 1. Comparison of often-used LIS models [12,20–25] to Voyager 1 (downward triangles), PAMELA (dots) and AMS02 (upward triangles) observations. The energy range most important for the production of the cosmogenic radionuclides is highlighted in grey. Figure adapted from Herbst *et al.* [12], reproduced with permission.

particle fluxes. This study focuses on investigating the significance of the local interstellar spectrum (LIS), geomagnetic field and atmospheric interaction models employed in the production of the cosmogenic radionuclides ^{10}Be, ^{14}C and ^{36}Cl to openly discuss the uncertainties that impact the numerically derived global production rate values.

2. Background

In the following, background information on (a) the LIS and its heliospheric modulation, (b) geomagnetic field models and its variations and (c) the numerical steps to model the cosmogenic radionuclide production rate values are highlighted.

(a) The local interstellar spectrum and its modulation

An important parameter in modelling the production of cosmogenic radionuclides is the so-called LIS, the unmodulated particle spectrum outside the heliosphere [11,12]. Until the end of 2012, the LIS had not been measured *in situ*, and thus multiple LIS models going back to the late 1970s exist in the literature. The models most commonly used have been shown to differ in the particle fluence by up to a factor of four [11,13], particularly in the energy regime below 30 GeV. However, with Voyager 1 crossing the heliopause at the end of 2012, it is commonly accepted that we are now measuring the unmodulated GCR spectrum at energies below 500 MeV [14,15], although the influence of the heliosphere on low-energy GCRs may still extend somewhat beyond the heliopause owing to interactions with the very local interstellar field, as well as transport conditions in the very local interstellar medium (e.g. [16,17]). Based on these measurements and observations of the Payload for Antimatter Matter Exploration and Light-nuclei Astrophysics (PAMELA, [18]) and AMS02 [19] instruments, new LIS models have been established [12,20–22].

Downloaded from royalsocietypublishing.org/rsta/article-pdf/doi/10.1098/rsta.2025.0348/6165301/rsta.2025.0348.pdf
by guest
on 14 September 2026

Figure 1 shows a comparison of often used LIS models to the Voyager 1 (black triangles), PAMELA (black dots) and AMS02 (blue triangles) observations. As can be seen, the choice of LIS model can change the particle flux by more than an order of magnitude at lower energies, particularly between the older models and the newer versions [12,20–22] that have been fixed to better match the Voyager data. However, within the energy range most important for the cosmogenic radionuclide production (shaded in grey), only low-energy observations of the LIS are available.

Nevertheless, as soon as GCRs enter the heliosphere, they are modulated by the HMF (see the PAMELA and AMS02 data in figure 1). Because of the modulation processes, during phases of low solar activity much higher particle intensities can be detected inside the heliosphere than during times of high solar activity. Thereby, the transport of GCRs in the heliosphere can be described by Parker's [26] transport equation.

Its three-dimensional representation is given by the following:

$$\frac{\partial f}{\partial t} = \nabla \cdot \left(\mathbf{K} \cdot \nabla f\right) - \mathbf{V}_{sw} \cdot \nabla f + \frac{1}{3}\left(\nabla \cdot V_{sw}\right)\frac{\partial f}{\partial \ln p}, \tag{2.1}$$

where f is the omnidirectional GCR distribution function, related to the differential intensity reported on from spacecraft observations by $j_T = p^2 f$, with p the particle momentum. The Parker equation models the influence of convection within a solar wind at speed V_{sw} (middle term on the right-hand side) and adiabatic energy changes (last term on the right-hand side), while diffusion and drift effects are represented by the diffusion tensor $\mathbf{K}$ (first term on the right-hand side). As discussed in [27], given in HMF-aligned coordinates, $\mathbf{K}$ is represented by

$$\mathbf{K}' = \begin{bmatrix} \kappa_{\perp,3} & \kappa_A & 0 \\ -\kappa_A & \kappa_{\perp,2} & 0 \\ 0 & 0 & \kappa_{\parallel} \end{bmatrix}. \tag{2.2}$$

Note that the subscripts on the diffusion coefficients κ indicate whether they describe diffusion parallel or perpendicular to the local HMF.

Equation (2.1) describes the time- and energy/momentum-dependent evolution of the GCR intensity in three dimensions and, ideally, should be solved accordingly, which necessitates numerical modelling. In the past decades, such modulation codes have become able to solve equation (2.1) to increasing degrees of refinement, taking into account more fundamental particle transport physics (see the review by Engelbrecht *et al.* [28]). However, such models are by their very nature complex and require considerable computation. As such, simpler approaches to solving the Parker equation are often sought and implemented.

A widely used but only zero-order approximation is the so-called force-field approach [29–32], derived by assuming a spherically symmetric heliosphere in a steady state with no local sources of CRs, considering only transport in the radial direction with an effective diffusion coefficient $\kappa(r, p)$ that is only dependent on momentum and radial distance. It does not explicitly account for adiabatic energy losses but mimics this process by taking into account the Compton–Getting effect [33,34]). As a result, the transport of charged particles depends only on one free parameter, the solar modulation parameter ϕ. The time-dependent differential GCR flux at 1 AU is given by

$$J(E, \phi) = J_{\mathrm{LIS}}(E + \Phi)\frac{(E)(E + 2E_r)}{(E + \Phi)(E + \Phi + 2E_r)}, \tag{2.3}$$

where J_{LIS} reflects the unmodulated GCR flux outside the heliosphere, E is the kinetic energy of the charged particles, E_r is the rest-mass energy of the CRs (for protons E_r ~938 MeV) and Φ is the modulation function given by $\mathrm{A/Z}\,\phi$, where A/Z is the ratio of the mass to atomic number for a particular species of GCR. Given a particular expression for the LIS, ϕ can then be calculated for a set of GCR observations at Earth. The resulting modulation parameters then display a clear solar cycle dependence, where low/high values go along with low/high solar activity, with the clear implication that ϕ depends on the various physical parameters that influence the solar cycle-dependent transport of GCRs. Extreme caution, however, needs to be taken when attempting to

Downloaded from royalsocietypublishing.org/rsta/article-pdf/doi/10.1098/rsta.2025.0348/6165301/rsta.2025.0348.pdf
by guest
on 14 September 2026

glean further information from ϕ as to the heliospheric plasma parameters (such as, for instance, the HMF magnitude or solar wind speed) that influence the transport and modulation of GCRs.

An alternative modulation parameter, M_{CD}, can be computed from the convection–diffusion approach. This is also a one-dimensional approach to solving the Parker transport equation, making the same assumptions as the force-field approach, but without taking into account the Compton–Getting effect [30,32]. The force-field and convection–diffusion modulation parameters can be related by assuming a separable effective diffusion coefficient, such that $\kappa(r, P) = \beta k_1(r) k_2(P)$ (with β the ratio of particle speed to the speed of light), is given by

$$\phi = \beta k_2 \frac{M_{CD}}{3} = \beta k_2 \frac{1}{3} \int_r^{r_b} \frac{V_{sw}}{\kappa(r, p)} \mathrm{d}r, \tag{2.4}$$

where r_b denotes the radial distance of the modulation boundary. It follows that a particular value of ϕ that yields a fit to observations must have an equivalent M_{CD}. However, information as to the heliospheric plasma parameters used to calculate M_{CD} is, in a sense, entangled in the integration: there is no way to distinguish between any combination of V_{sw}, $\kappa(r, p)$ or r_b that, when integrated, happen to yield the required value for M_{CD} (and hence ϕ). Some parameter combinations may be eliminated based on spacecraft observations, but these are limited, and were unavailable prior to the space age. There is also a choice of LIS implicit to any reported value of ϕ, as can be seen from equation (2.3). Therefore, the use of different LIS models will lead to LIS-dependent modulation parameters that then have to be converted to each other by means of linear regression functions, a process which has a strong influence on the computation of the cosmogenic radionuclide production rates [11,12].

Furthermore, as discussed in §2c, owing to their different production mechanisms, ^{10}Be, ^{14}C and ^{36}Cl are not equally sensitive to changes in the low-energy part of the modulated LIS; thus, differences in the production during solar maximum conditions will occur. A reconstruction of the values of the monthly modulation parameter based on ionization chambers and neutron monitor (NM) measurements has been performed [35]. However, Corti *et al*. [22] and Gieseler *et al.* [36] revealed inconsistencies between these NM-based modulation values and actual measurements by, for example, PAMELA [18] and AMS02 [19]. It was shown that a rigidity-dependent solar modulation parameter is mandatory to describe the GCR modulation when applying the force-field approximation [36]. However, to derive a physically consistent description of the rigidity- and charge-dependent modulation throughout the heliosphere and produce a near-Earth GCR spectrum that is suitable as input for the cosmogenic radionuclide production calculations, a three-dimensional treatment of the transport equation is essential. This is because the above-mentioned assumptions made in the derivations of both the force-field and convection–diffusion approaches preclude the physically correct modelling of several GCR transport mechanisms, such as drift effects (e.g. [37,38]) and three-dimensional diffusion (which makes an important distinction between diffusion parallel and perpendicular to the HMF, see [28,39–41]), which are known to play significant roles in GCR modulation [28,42,43]. Nevertheless, until today, the simplified force-field solution has set the baseline for the reconstruction of the solar activity on time scales of thousands of years, an inconsistency that probably has a non-negligible influence on the modelled ^{10}Be, ^{14}C and ^{36}Cl production rate values.

(b) The geomagnetic field variations

CRs approaching Earth will interact with its magnetic field. The magnetic field components, thereby, alter their trajectories. The field can be approximated by a dipole with an axis inclined approximately 11° relative to the Earth's rotational axis and displaced from it; its orientation is also antipodal to the rotational axis. The magnetosphere spans approximately 6 to 12 Earth radii in the nose direction towards the Sun. This distance is strongly influenced by the HMF, the speed/density of the solar wind and other space weather phenomena, like CME. In the tail

Downloaded from royalsocietypublishing.org/rsta/article-pdf/doi/10.1098/rsta.2025.0348/6165301/rsta.2025.0348.pdf
by guest
on 14 September 2026

direction, the magnetosphere extends up to a thousand Earth radii. The motion of CRs—being charged particles—within a magnetic field is characterized by three components: a spiral trajectory, a north-south movement and an east-west drift along these lines. Thus, the geomagnetic field influence on charged particles is twofold: (i) the trajectory of the incoming particle is curved, resulting in an arrival direction that differs from that in the absence of a magnetic field, and (ii) the magnetic field acts as an energy filter that prevents low-energy CRs from penetrating to the surface. The minimum rigidity threshold of a particle required to reach a certain location within the Earth's atmosphere is referred to as the geomagnetic rigidity cutoff (R_C). Particles with a rigidity below this cutoff are confined within the magnetic field while those particles with much lower rigidities are deflected into interplanetary space. Størmer [44] characterized the geomagnetic rigidity cutoff in the following way:

$$R_C = \frac{M}{r^2} \frac{\cos^4 \lambda}{\left[1 + \left(\sqrt{1 - \sin\vartheta \sin\varphi \cos^3 \lambda}\right)^{\frac{1}{2}}\right]^2}, \tag{2.5}$$

where M is the dipole moment, λ represents the geomagnetic latitude, ϑ is the zenithal, φ is the azimuthal angle and r is the distance from the dipole centre. Approaching $\cos\lambda \to 0$, equation (2.5) can be re-written as

$$R_C = \frac{M \cdot \cos^4 \lambda}{4 \cdot r^2}. \tag{2.6}$$

As it is an easy-to-use expression, equation (2.6) is widely used in the literature. However, strictly speaking, this expression is only valid at high latitudes [44,45]. A more realistic description is given by the international geomagnetic reference field (IGRF, [46]). Mathematically speaking, it describes the main geomagnetic field $\mathbf{B}(r, \theta, \phi, t)$ as the gradient of a scalar potential ($\mathbf{B} = -\nabla V$). Thereby, the potential $V(r, \theta, \phi, t)$ is given as

$$V(r, \theta, \phi, t) = a \sum_{n=1}^{N} \left(\frac{a}{r}\right)^{n+1} \sum_{m=0}^{n} \left[g_n^m(t) \cos(m\phi) + h_n^m(t) \sin(m\phi)\right] P_n^m(\cos\theta), \tag{2.7}$$

where r is radial distance from the Earth's centre, a is the Earth's reference radius ($a \approx 6371.2$ km), N is the maximum degree of the IGRF expansion (e.g. $N = 13$ for recent epochs), $g_n^m(t)$ and $h_n^m(t)$ are the (time-dependent) Gauss coefficients, tabulated by the IGRF model, P_n^m are the associated Legendre functions, θ is the colatitude ($\theta = 0$ at the north pole and $\theta = \pi/2$ at the geographic equator) and ϕ is the geographic longitude.

The production of the cosmogenic radionuclides is anti-correlated with the geomagnetic field intensity. Internally driven geomagnetic field changes are likely to play a significant role on time scales of 500 years and longer [47,48]. However, reconstructing changes in the dipole moment beyond historical observations is one of the most challenging tasks in computing the geomagnetic field [49]. Consequently, internal geomagnetic field variations can be seen as one of the major uncertainties in reconstructing recent as well as ancient solar activity changes. To determine the dipole moment, regional differences in geomagnetic field intensities have to be filtered out on the basis of good global data coverage that is currently unavailable for the Holocene and earlier periods.

The upper panel of figure 2 shows a comparison of the virtual axial dipole moments (VADMs) derived from different groups [50–54]. Despite the uncertainties owing to the use of different model approaches, an overall good agreement is present in the long-term trend of the different geomagnetic field reconstructions. Note that this trend is gradually decreasing towards present conditions and that more recent times (e.g. –50 to 50 BP) are represented by calculations based on the IGRF. In spite of the overall good agreement, it has to be mentioned that the data for these global geomagnetic field models mainly arise from the northern hemisphere, leading to

Downloaded from royalsocietypublishing.org/rsta/article-pdf/doi/10.1098/rsta.2025.0348/6165301/rsta.2025.0348.pdf
by guest
on 14 September 2026

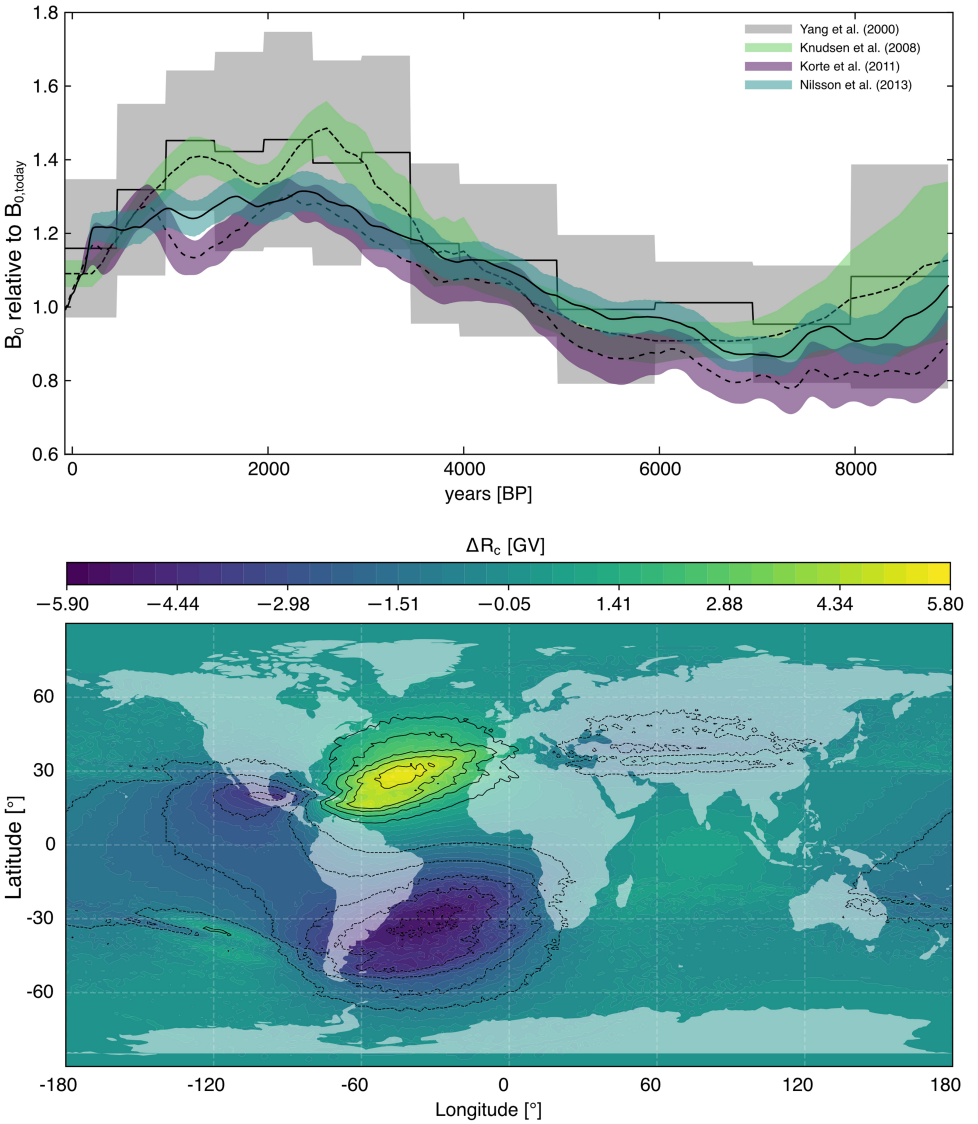


Figure 2. Upper panel: virtual axial dipole moments (VADM) reconstructions for the Holocene derived from Yang *et al.* [50] (grey), Korte *et al.* [51] (blue) and the more recent archaeomagnetic field models by Licht *et al.* [52] (green), Knudsen *et al.* [53] (red) and Nilsson *et al.* [54] (light blue). Lower panel: differences in the vertical cutoff rigidities between the values calculated for 1900 and 2026. Dark colours refer to rigidity decreases (i.e. at the location of the South Atlantic Anomaly and Mexico), and light colours refer to rigidity increases (mid-North Atlantic).

potential biases in these VADM reconstructions [55]. Nilsson *et al.* [55] found that long-term differences between Greenland and Antarctic ^{10}Be as well as tree-ring ^{14}C records can largely be resolved by including possible northern and southern hemisphere differences in the geomagnetic shielding.

Despite the long-term changes of the geomagnetic field, short-term changes may also have an influence on the production of the cosmogenic radionuclides. The lower panel of figure 2 shows the changes in cutoff rigidity for a particle to reach 20 km and below, between 1900 and 2026 (e.g. [13,56]). As can be seen, location-dependent changes of up to ±6 GV occurred over the past

Downloaded from royalsocietypublishing.org/rsta/article-pdf/doi/10.1098/rsta.2025.0348/6165301/rsta.2025.0348.pdf
by guest
on 14 September 2026

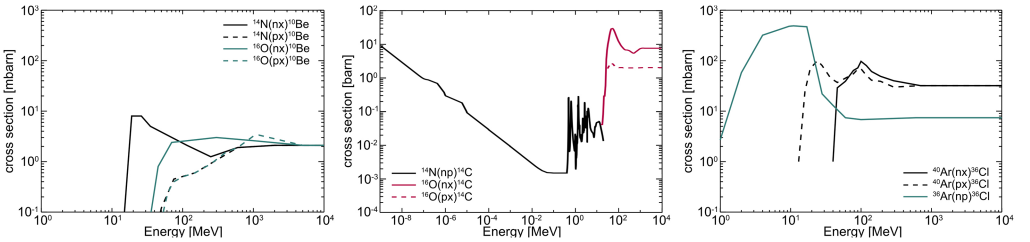


Figure 3. Energy-dependent cross-sections as a function of particle energy. Left-hand panel: for ^{14}N(n/px)^{10}Be in black and ^{16}O(n/px)^{10}Be in green, data taken from Masarik & Beer [59]. Middle panel: for ^{14}N(np)^{14}C (in black) based on the Joint Evaluated Fission and Fusion (JEFF) Nuclear Data Library, ^{16}O(nx)^{14}C (red solid line) by Michel *et al.* [60], and ^{16}O(px)^{14}C (red dashed line) by Reedy [61]. Right-hand panel: for ^{40}Ar(n/px)^{36}Cl in black and ^{36}Ar(np)^{36}Cl in green, data by Beer *et al.* [62].

116 years.[1] Overall, such short- and long-term changes might trigger significant and thus non-negligible differences in the computations of the global radionuclide production rates.

(c) Atmospheric interactions and production

Particles that are able to enter the terrestrial atmosphere will interact with the atmospheric environment. While low-energy particles mainly lose energy owing to ionization processes in the upper atmosphere, the interaction of high-energy primary particles deeper inside the atmosphere leads to the evolution of altitude-dependent secondary particle cascades mainly consisting of secondary neutrons, protons and muons. Of great importance for the production of both short- and long-lived cosmogenic radionuclides, in particular, are secondary neutrons and protons.

Numerically, the production, P, of a radionuclide of type j can be derived as

$$P_j(E_p, x) = \sum_i N_i \int_{E_C}^{\infty} \frac{\mathrm{d}F_p}{\mathrm{d}E_p \mathrm{d}t} \mathrm{d}E_p \sum_k \int_0^{\infty} \sigma_{ijk}(E_k) \cdot J(E_p, E_k, x) \mathrm{d}E_k, \tag{2.8}$$

where N_i represents the density of the target atom of species i, E_k represents the energy of the secondary particle of type k, $\mathrm{d}F_p/(\mathrm{d}E_p\mathrm{d}t)$ represents the differential primary particle fluence rate on top of the atmosphere and $f(E_p, E_k, x)$ represents the secondary particle fluence at a specific atmospheric depth x [13,57,58]. Moreover, σ_{ijk} represents the cross-sections for the production of the cosmogenic radionuclide of type j. Figure 3 shows the corresponding excitation functions for the production of ^{10}Be (left-hand panel), ^{14}C (middle panel) and ^{36}Cl (right-hand panel). Each of the cross-sections has a specific threshold energy that is an indicator of the minimum energy required to trigger the corresponding reaction. As can be seen, the cross-sections for the production of ^{10}Be and ^{36}Cl, both produced by spallation reactions, are restricted to an energy range between 0.01 and 10 GeV. For the production of ^{14}C, produced by thermal neutron capture, however, much lower energies within 10^{-12}–0.1 GeV are important. Because cross-sections are not well-known, it may not be as surprising that, for example, for the production of ^{10}Be, several sets of cross-sections exist in the literature. The radionuclide production equation can also be written as

$$P_j(E_p, x) = \int_{E_C}^{\infty} \frac{\mathrm{d}F_p}{\mathrm{d}E_p \mathrm{d}t} \mathrm{d}E_p \cdot Y_j(E_p, x), \tag{2.9}$$

[1]Note that these changes have become increasingly more rapid over the past three decades: within the past 10 years, changes of up to ±1 GV occurred in the mid-North Atlantic regions, within the South Atlantic Anomaly and in Mexico.

Downloaded from royalsocietypublishing.org/rsta/article-pdf/doi/10.1098/rsta.2025.0348/6165301/rsta.2025.0348.pdf
by guest
on 14 September 2026

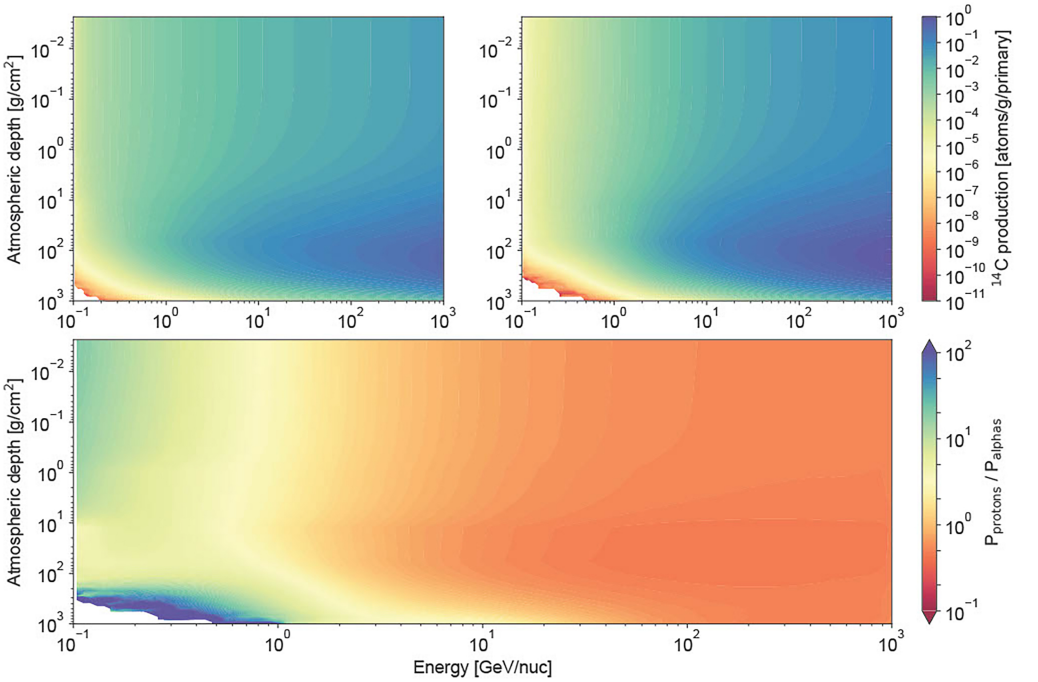


Figure 4. Upper panels: ^{14}C production by primary hydrogen (left) and helium (right) as a function of primary particle energy and the atmospheric depth. Lower panel: ratio between the ^{14}C production owing to primary protons and primary alpha particles.

where the primary particle energy and altitude-dependent yield function $Y(E_p, x)$ reveal information about the number of cosmogenic nuclides of species j, which are produced owing to a single primary particle of type p with an energy E_p. Further, E_C is the cutoff energy, the minimum energy a particle must have in order to be able to reach a certain location at a specific atmospheric depth/altitude, that can be converted to the so-called cutoff rigidity R_C.

Using codes such as the GEANT4 [63] based PLANETOCOSMICS [64], the interactions of the primary protons and alpha particles with the surrounding atmospheric material can be computed. For example, the panels of figure 4 show the production rates of ^{14}C per primary proton (left) as well as primary alpha particles (right) at depths ranging from 100 MeV to 1 TeV as a function of atmospheric depth between 0.002 and 1024.8 g cm^{-2}. The higher the energy of the primary particle, the deeper the particle is able to penetrate into the atmosphere to deposit energy. For further information on the ^{10}Be production rates, the reader is referred to Matthiä *et al.* [57].

As a consequence, the ^{14}C production per primary incident particle increases with increasing primary particle energy. In addition, for high-energy incident particles, a production maximum at an atmospheric depth around 150–200 g cm^{-2} is reached. Beyond this depth, the yield begins to decline as fewer particles can penetrate to these depths to induce further secondary particle production. Furthermore, primary alpha particles produce more ^{14}C atoms cm^{-1} compared to primary protons, and in both scenarios, primary particle energies below a few hundred MeV contribute only marginally to the production of cosmogenic radionuclides. It further becomes apparent that the production owing to primary alpha particles is higher at atmospheric depths below the production maximum than owing to primary protons [13,57].

The upper panel of figure 5 shows the ^{14}C yield functions at atmospheric depths between 0.023 (in yellow) and 1025 g cm^{-2} (in purple). In addition, the lower panel of figure 5 shows a comparison

Downloaded from royalsocietypublishing.org/rsta/article-pdf/doi/10.1098/rsta.2025.0348/6165301/rsta.2025.0348.pdf
by guest
on 14 September 2026

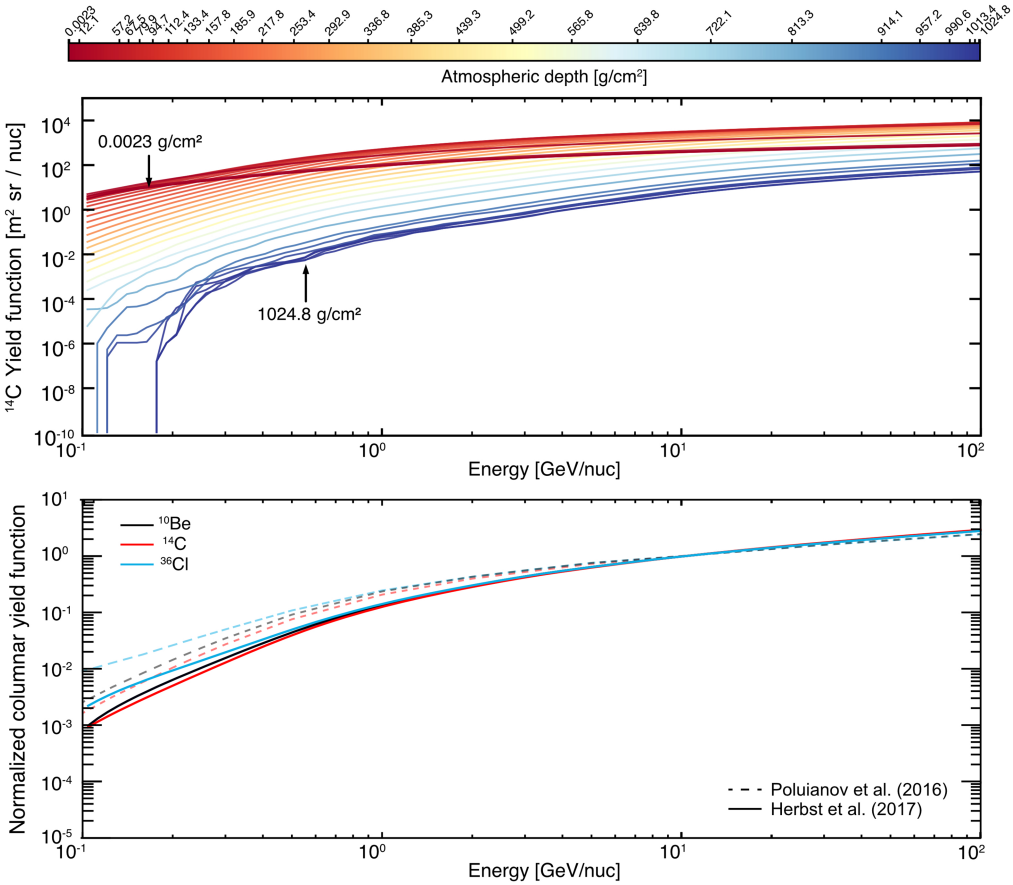


Figure 5. Upper panel: depth-dependent ^{14}C yield functions as a function of primary particle energy (i.e. $Y_j(E_p, x)$) at atmospheric depths between 0.023 and 1025 g cm^{-2}. Lower panel: corresponding columnar yield functions of ^{10}Be, ^{14}C and ^{36}Cl normalized to 10 GeV nuc^{-1}. Here, a comparison between the yield functions based on Herbst *et al.* [12] (solid lines) and Poluianov *et al.* [65] (dashed lines) is shown.

of the columnar yield functions of ^{10}Be (black line), ^{14}C (red line) and ^{36}Cl (blue line) normalized to 10 GeV. Solid lines show the results based on the modelling by Herbst *et al.* [12], while the dashed lines present those of Poluianov *et al.* [65]. As can be seen, only minor differences occur between the three yield functions at high energies. However, in the low-energy ranges, they differ by an order of magnitude. Note that at lower energies, the production rate of the long-lived radionuclide ^{36}Cl shows much higher yield function values than that of ^{14}C and ^{10}Be. As a consequence, ^{36}Cl is much more sensitive than ^{10}Be or ^{14}C to lower-energy particles, particularly during so-called ground level enhancement events, which are strong solar particle events energetic enough to reach the Earth's surface.

By folding the yield functions with a primary particle spectrum, the response function $R_j(E_p, x)$ [66] can be computed:

$$R_j(E_p, x) = \frac{\mathrm{d}F_p}{\mathrm{d}E_p \mathrm{d}t} dE_p \cdot Y_j(E_p, x). \tag{2.10}$$

The energy-dependent ^{10}Be, ^{14}C and ^{36}Cl response functions for primary GCRs as a function of the solar modulation parameter ϕ, varying between 0 to 2000 MV, are shown in the first three panels of figure 6, respectively.

Downloaded from royalsocietypublishing.org/rsta/article-pdf/doi/10.1098/rsta.2025.0348/6165301/rsta.2025.0348.pdf
by guest
on 14 September 2026

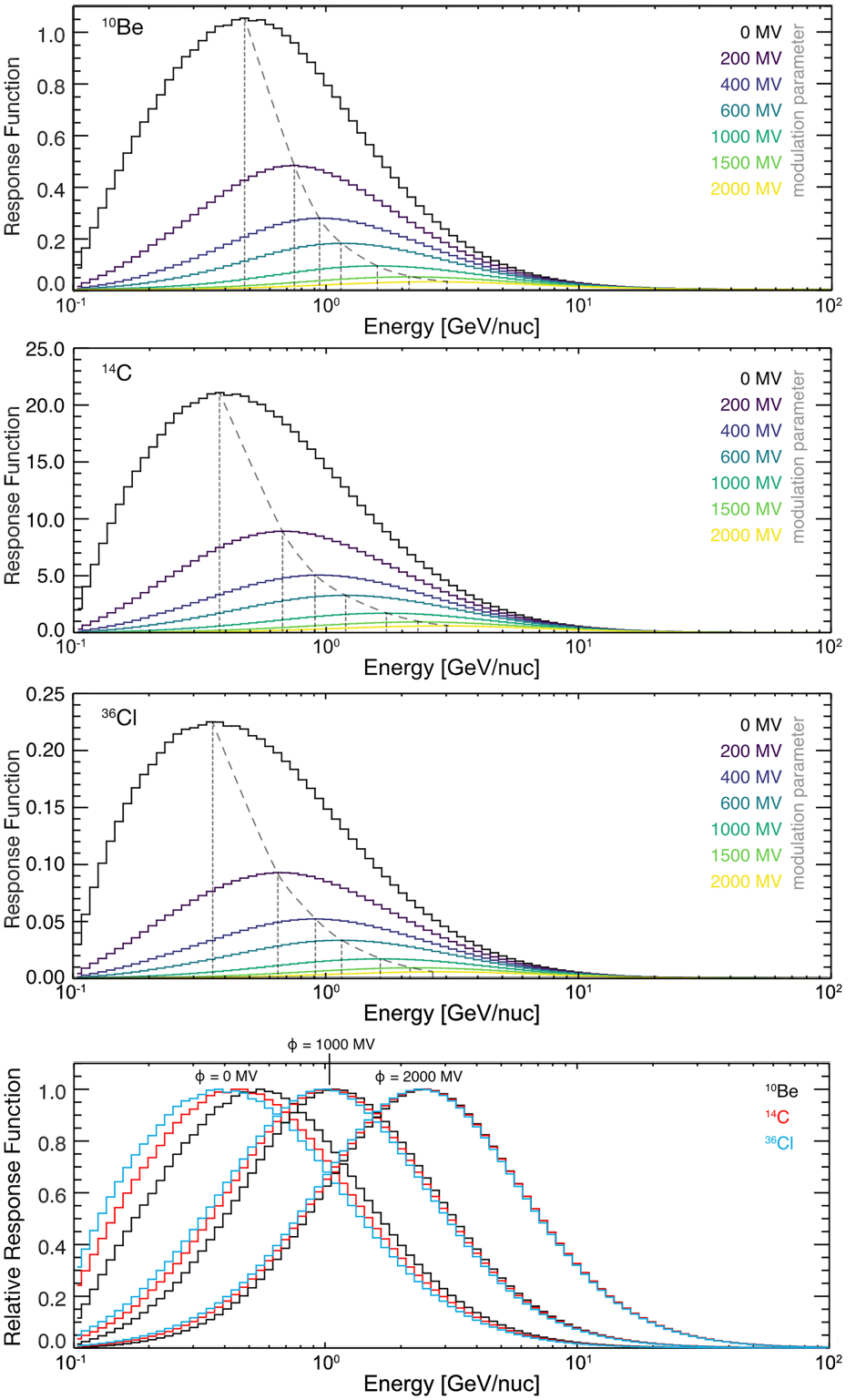


Figure 6. Upper three: response functions of the production of ^{10}Be, ^{14}C and ^{36}Cl depending on the solar modulation parameter varying from unmodulated values (i.e. 0 MV) and solar maximum conditions (i.e. 2000 MV). Lower panel: relative response function of ^{10}Be (in black), ^{14}C (in red) and ^{36}Cl (in blue) for low, moderate and high modulation parameter values, respectively.

Downloaded from royalsocietypublishing.org/rsta/article-pdf/doi/10.1098/rsta.2025.0348/6165301/rsta.2025.0348.pdf
by guest
on 14 September 2026

As discussed in §2a, the activity-dependent GCR spectrum typically shows an intensity variation below 30 GeV nuc^{-1} and an intensity maximum around 1 GeV nuc^{-1} (for $\phi >$ 0 MV), which causes the production maximum of the response functions to shift towards much higher energies with increasing solar activity (i.e. higher ϕ values). In addition, the lower panel shows the corresponding relative response functions of all three radionuclides for three modulation values reflecting no modulation (ϕ = 0 MV), medium conditions (i.e. ϕ = 1000 MV) and very strong solar modulation (i.e. ϕ = 2000 MV). With increasing solar activity (so with increasing ϕ-values), the response maximum of all three radionuclides shifts towards higher energies.

The presented simulations are based on the GEANT4 Monte Carlo software version 4.9.1 [63] integrated in the PLANETOCOSMICS tool [64]. The model runs are based on the hadronic interaction model QGSP_BERT_HP and the GEANT4 interface to the JAM/JQMD model by Koi et al. [67] to include the inelastic nuclear scattering of helium or heavier nuclei at energies above 10 GeV nuc^{-1}.

Because ^{36}Cl is more sensitive to changes in the low-energy range, the maximum of its response function is shifted to lower energies during solar minimum conditions. Because of that, strong SEP events with soft spectra—showing orders-of-magnitude higher differential intensities at lower energies but lower intensities at higher energies compared to SEP events characterized by hard spectra—are more likely to be detected in ^{36}Cl rather than in ^{10}Be or ^{14}C records [10,58].

3. Discussion

In what follows, we assess the numerical uncertainties coupled to the following questions: how much do different LIS models impact the response functions? How much do different estimates of cross- sections impact the expected ^{10}Be, ^{14}C and ^{36}Cl production? Are computations based on different magnetic field models comparable?

(a) Response functions and their dependence on the local interstellar spectrum model

Response functions strongly depend on the high-energy spectrum triggering the atmospheric response. Thus, using different LIS models (see §2a) leads to differences in the modelled atmospheric response functions and, in the end, also the modelled local and global cosmogenic radionuclide production rates. Exceptionally, the upper panel of figure 7 shows the response functions of ^{10}Be using the LIS models by Usoskin *et al.* [25] (black lines) and Herbst *et al.* [12] (blue lines). As shown in figure 1, the latter is in much better agreement with the low-energy Voyager observations and, with that, provides a more realistic representation of the GCR proton spectrum. As can be seen, the maximum of the response function varies between the two models, being shifted to higher energies when applying the LIS by Herbst *et al.* [12]. For better comparison, the lower panel shows the residuals of the response functions based on Herbst *et al.* [12] relative to Usoskin *et al.* [25]. As can be seen, using different LIS models results in strong differences in the atmospheric response function.

While the response functions based on Herbst *et al.* [12], overall, result in larger values in the low-energy range up to 7 GeV nuc^{-1}, for energies above they are up to 100% smaller than those resulting from the use of the LIS by Usoskin *et al.* [25]. The impact on the local and global cosmogenic radionuclide production is discussed in the following.

Using the observation-based LIS model by Herbst et al. [12] leads to response functions up to 20% larger than those using the LIS model by Usoskin et al. [25] in the energy range most important for the production of ^{10}Be, ^{14}C and ^{36}Cl (grey box, lower panel of figure 7).

Downloaded from royalsocietypublishing.org/rsta/article-pdf/doi/10.1098/rsta.2025.0348/6165301/rsta.2025.0348.pdf
by guest
on 14 September 2026

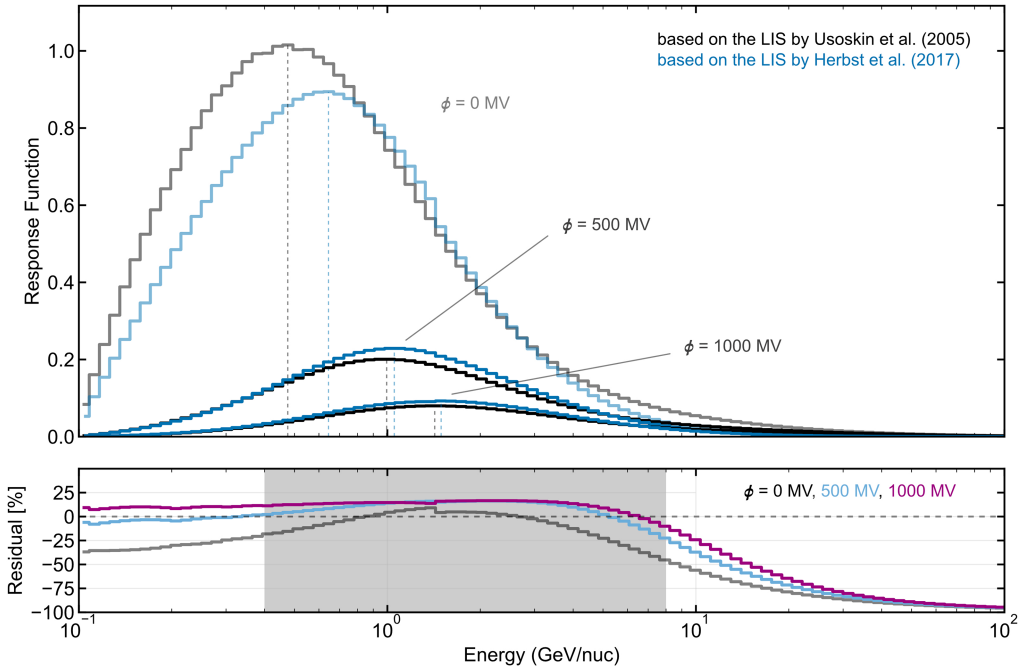


Figure 7. Upper panel: response function of ^{10}Be for unmodulated times ($\phi = 0$ MV), solar minimum conditions ($\phi = 500$ MV) and solar maximum conditions ($\phi = 1000$ MV). Response functions are shown for different LIS spectra: Usoskin *et al.* [25] in black and Herbst *et al.* [12] in blue. Lower panel: residuals of the response function based on the LIS by Herbst *et al.* [12] relative to the one based on Usoskin *et al.* [25] for $\phi = 0$ MV (in black), $\phi = 500$ MV (in blue) and $\phi = 1000$ MV (in purple).

(b) Local and global production rate values

To calculate the production rates at a specific location, the geomagnetic shielding and its dependencies (§2b) need to be taken into account. The local production rate, depending on the solar activity and a given location (i.e. cutoff rigidity), is given by the atmospheric depth-integrated production rates numerically described as

$$P_{\text{local}}(\phi, R_C) = \int_x P(\phi, R_c, x)\, \mathrm{d}x. \tag{3.1}$$

The production mechanisms, and consequently the cross-sections, differ among isotopes, yet, as shown in the upper panels of figure 8, the local production rates of ^{10}Be (left), ^{14}C (middle) and ^{36}Cl (right) as a function of cutoff rigidity ranging from 0 to 17 GV[2] exhibit similar trends: (i) lower solar modulation correlates with higher local production rates, and (ii) the modulation effect is most pronounced in areas with low cutoff rigidity values, particularly in polar regions (i.e. $R_C \approx 0$ GV), while it is nearly negligible in areas with high cutoff rigidity values, especially in equatorial regions ($R_C \geq 15$ GV).

Global-averaged production is often used instead of local production because atmospheric transport and deposition processes mix local variations. For example, previous studies suggest that deposition reflects relative changes caused by solar modulation, consistent with those indicated by global-averaged production rates [68,69]. To derive the mean global cosmogenic radionuclide production, which—among others—depends on the solar modulation parameter, equation (3.1) has to be integrated over all locations. An in-depth discussion of the approach is given in chapter 7 of [13]. For example, the upper panel of figure 9 shows a comparison of the

[2]The values are in line with current IGRF-based ranges.

Downloaded from royalsocietypublishing.org/rsta/article-pdf/doi/10.1098/rsta.2025.0348/6165301/rsta.2025.0348.pdf
by guest
on 14 September 2026

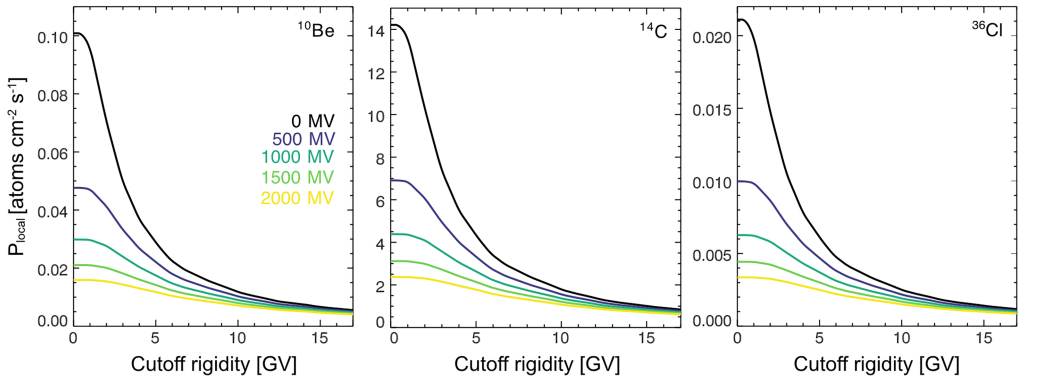


Figure 8. Local production rates of ^{10}Be (left), ^{14}C (middle) and ^{36}Cl (right) as function of the cutoff rigidity R_C during varying solar activity ranging between 0 and 2000 MV.

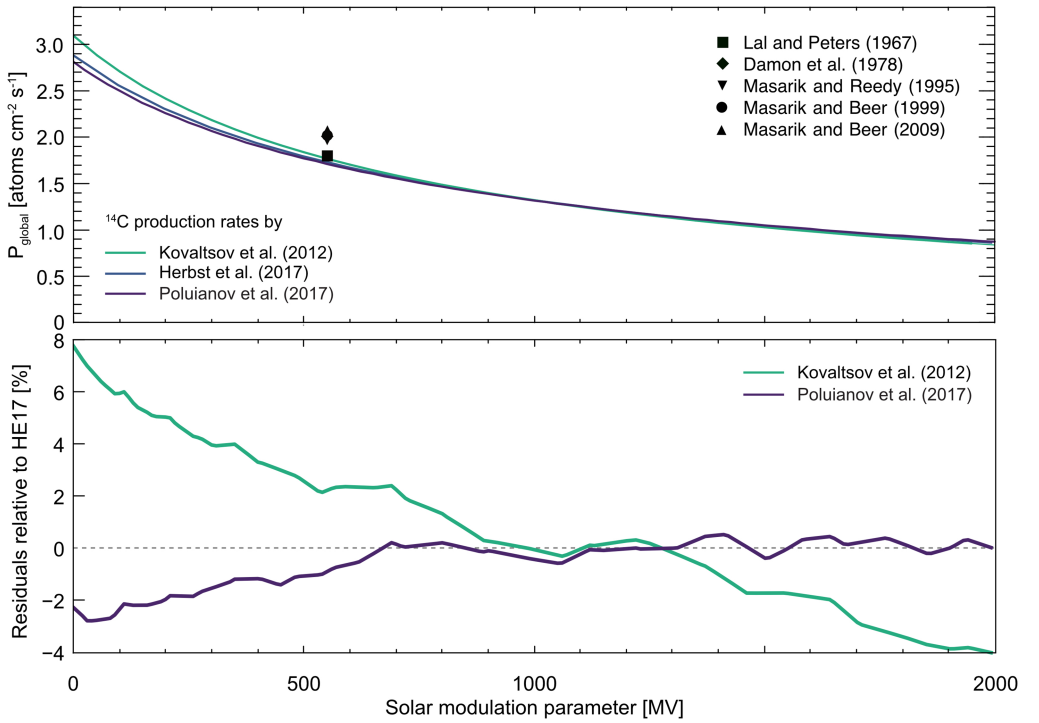


Figure 9. Upper panel: comparison of the globally averaged ^{14}C production rate model results by Lal & Peters [70], Damon *et al.* [71], Masarik & Reedy [72], Masarik & Beer [59] and Masarik & Beer [73] for $\phi = 550$ MV and as a function of the solar modulation parameter ϕ based on the model efforts by Kovaltsov *et al.* [74], Herbst *et al.* [12] and Poluianov *et al.* [65]. Note that the latter three are based on the same LIS model. Lower panel: residuals of the global production rates by Kovalsov *et al.* [74] and Poluianov *et al.* [65] relative to the model results by Herbst *et al.* [12].

modelled global ^{14}C production rates at a solar modulation of $\phi = 550$ MV of the pioneering works by Lal & Peters [70], Damon *et al.* [71], Masarik & Reedy [72], Masarik & Beer [59] and Masarik & Beer [73] (black symbols) and the model efforts by Kovaltsov *et al.* [74] (in green), Poluianov *et al.* [65] (in purple) and Herbst *et al.* [12] (in blue) covering modulation parameter values between 0 and 2000 MV. As can be seen, the latest works (i.e. [12,65,74]) are in good agreement with the value derived by Lal & Peters [70]. It further shows that the newest model efforts agree well in moderate to high solar activity phases (i.e. above 500 MV), while differences of up to 8% occur at

Downloaded from royalsocietypublishing.org/rsta/article-pdf/doi/10.1098/rsta.2025.0348/6165301/rsta.2025.0348.pdf
by guest
on 14 September 2026

Table 1. Model set-up of the numerical efforts to derive the ^{14}C production rates.

Study	LIS model	physics list	cross-sections	energy range
Kovaltsov *et al.* [74]	Usoskin *et al.* [25]	QGSP_BIC_HP	EXFOR/CSISRS	0.1–100 GeV
Poluianov *et al.* [65]	Usoskin *et al.* [25]	QGSP_BIC_HP	[75], [76], [77], [24], [62], [78], EXFOR/CSISRS[a]	0.02–100 GeV
Herbst *et al.* [12]	Herbst *et al.* [12]	QGSP_BERT_HP	[59]/ [62]	0.1–100 GeV

[a]The paper presents model results of different cosmogenic radionuclides and lists these references. It is not specifically stated which sources were used to model the ^{14}C production.

lower values between the results by Herbst *et al.* [12], Kovaltsov *et al.* [74] and Poluianov *et al.* [65] (see lower panel of figure 9). Differences of more than 10% occur between the results by Kovaltsov *et al.* [74] and Poluianov *et al.* [65] (not shown). However, a direct comparison of such absolute values should always be treated with caution, as crucial numerical inputs such as the used LIS model, cross-sections and magnetic field models are different (table 1) or—as is the case particularly for the earliest efforts—missing. Note that the presented studies are based on two different GEANT4 physics lists:[3] *QGSP_BIC_HP* and *QGSP_BERT_HP*. Matthiä [79], however, showed that observed secondary proton and neutron spectra—key for the production of ^{10}Be, ^{14}C and ^{36}Cl—are better represented using the *QGSP_BERT_HP* model.

(i) Dependence on the local interstellar spectrum model

The LIS plays a crucial role in the numerical description of the cosmogenic radionuclide production and, with that, the radionuclide-based reconstruction of the solar modulation parameter on long time scales [80]. The upper panel of figure 10 shows the computed global ^{10}Be production rate values using the LIS models by Usoskin *et al.* [25] (purple), Bisschoff & Potgieter [21] (yellow), Corti *et al.* [22] (green) and Herbst *et al.* [12] (blue). The lower panels show the same analysis for ^{14}C (left) and ^{36}Cl (right).

As indicated, the absolute production rate values vary by up to 30% during periods of low solar activity and by up to 15% during phases of high solar activity. Thereby, the LIS-dependent radionuclide production rates show different sensitivities to the solar activity changes, with ^{36}Cl being most sensitive to such variations, followed by ^{14}C and ^{10}Be, resulting from the production itself, which, particularly in the case of ^{36}Cl, is more sensitive to changes in the low-energy range and thus to the solar modulation. Nevertheless, the same characteristic occurs: the lower the solar activity, the larger the differences between the LIS-dependent production rate values. Surprisingly, the differences of 20–25% between the values based on the LIS from Bisschoff & Potgieter [21] and Herbst *et al.* [12] seem to be independent from the type of the radionuclide. However, as discussed in Herbst *et al.* [11,12], LIS-dependent modulation parameters have to be applied to directly compare the modelled production rate values, which significantly reduces the differences. Therefore, the latter strongly suggests that reconstructions of the solar modulation based on radionuclide records are much more robust if relative production rate computations are taken into account [12,80].

Not using the LIS-dependent modulation parameter values results in up to 20–30% difference in the production rate values, depending on the radionuclide of interest.

[3]http://geant4-userdoc.web.cern.ch/UsersGuides/PhysicsListGuide/html/physicslistguide.html.

Downloaded from royalsocietypublishing.org/rsta/article-pdf/doi/10.1098/rsta.2025.0348/6165301/rsta.2025.0348.pdf
by guest
on 14 September 2026

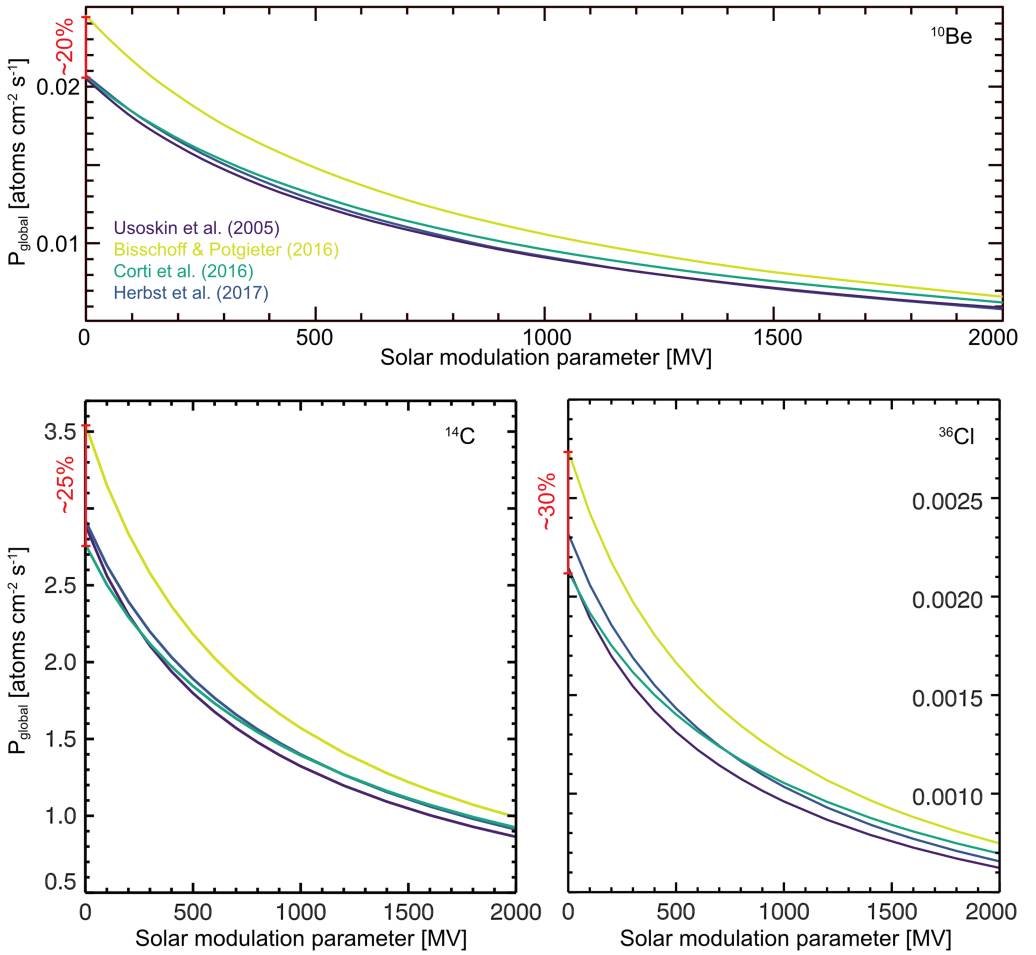


Figure 10. Dependence of the rates on the LIS model used to compute the ^{10}Be (upper panel, after Herbst *et al.* [12], reproduced with permission), ^{14}C (lower left) and ^{36}Cl (lower right) production. LIS models from Usoskin *et al.* [25] (in purple), Bisschoff & Potgieter [21] (in yellow), Corti *et al.* [22] (in green) and Herbst *et al.* [12] (in blue) have been used.

(ii) Dependence on the cross-sections

Numerically derived production rates further depend strongly on the cross-sections used in the computations [13,57]. However, although playing a crucial role, these cross-sections are not well-constrained. In fact, either only minor information on the excitation functions is available (^{14}C) or multiple neutron and proton cross-section sets exist in the literature (e.g. ^{10}Be). In addition, most neutron cross-sections above 100 MeV are estimated rather than measured [81]. Thus, the availability of reliable cross-sections remains a major limiting factor for cosmogenic radionuclide production models.

The upper panel of figure 11 shows the solar modulation parameter dependent local ^{10}Be production rate values based on the ^{14}N(n/p,x)^{10}Be and ^{16}O(n/p,x)^{10}Be cross-section datasets by Masarik & Beer [59] (solid lines) and Webber & Higbie [24] (dashed lines) shown in the two smaller inserted figures on the right-hand side. As can be seen, the local production rates based on Masarik & Beer [59] result in higher production rate values over the entire solar modulation range between 0 and 2000 MV. In particular, for cutoff rigidities below 13 GV, significant differences of up to 25% between the cross-section-dependent production rate values occur.

Downloaded from royalsocietypublishing.org/rsta/article-pdf/doi/10.1098/rsta.2025.0348/6165301/rsta.2025.0348.pdf
by guest
on 14 September 2026

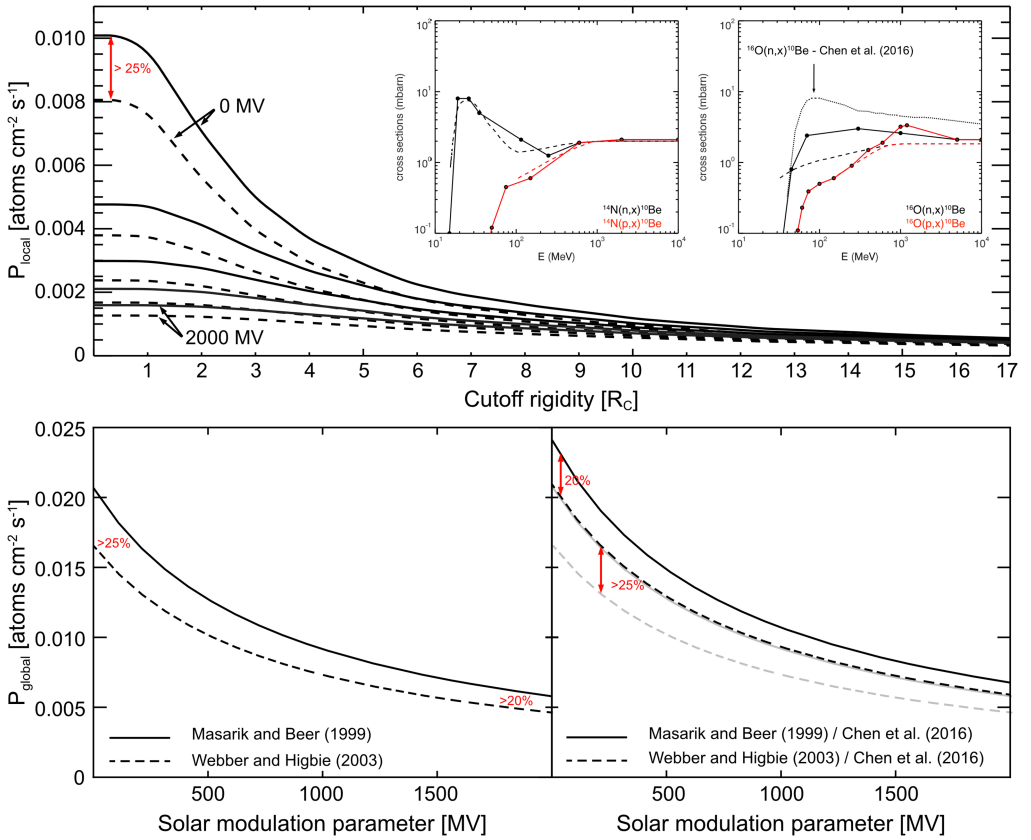


Figure 11. Local (upper panel) and global (lower panels) ^{10}Be production rates based on the cross-sections by Masarik & Beer [59] (solid lines) and Webber & Higbie [24] (dashed lines). For direct comparison, the grey lines show the results of the left-hand panel.

The lower panels of figure 11 show the corresponding global production rates. On the left, a comparison of the results for the original cross-section by Masarik & Beer [59] and Webber & Higbie [24] is shown. As can be seen, in low solar activity phases, the differences are still above 25% and even for high solar activity values, the differences account for more than 20%.

Recently, new ^{16}O(n,x)^{10}Be cross-sections have been published by Chen *et al.* [82] (dotted line in the upper panel of figure 11). Replacing the old ^{16}O(n,x)^{10}Be cross-sections of Masarik & Beer [59] and Webber & Higbie [24] with these new values reveals a significant underestimation of the production rate computations based on the old records. As can be seen in the lower right-hand panel of figure 11, the production rate values based on Webber & Higbie [24] are underestimated by almost 30%, while smaller changes can be seen in case of the production rate computations based on Masarik & Beer [59]. The reason for this is in the cross-sections themselves, as the new ^{16}O(n,x)^{10}Be values are closer to those of Masarik & Beer [59] than the ones published in Webber & Higbie [24]. The Joint Evaluated Fission and Fusion nuclear data library[4] ^{14}N(np)^{14}C values (black line) and the ^{16}O(n/px)^{14}C values by Michel [60] (dark-red lines) presented in the middle panel of figure 3 have also been re-measured. While Reedy [61] published a new excitation function for the ^{16}O(nx)^{14}C production, Wallner *et al.* [83] published new results for the ^{14}N(np)^{14}C cross-section in the energy range between 0.001 and 0.4 MeV. Although there are strong differences between old and new cross-section values at higher energies, ^{14}C is mainly produced by thermal neutron capture, and is thus most responsive to energies well below the respective energies. Thus,

[4]http://databank.io.oecd-nea.org/data/overview/.

Downloaded from royalsocietypublishing.org/rsta/article-pdf/doi/10.1098/rsta.2025.0348/6165301/rsta.2025.0348.pdf
by guest
on 14 September 2026

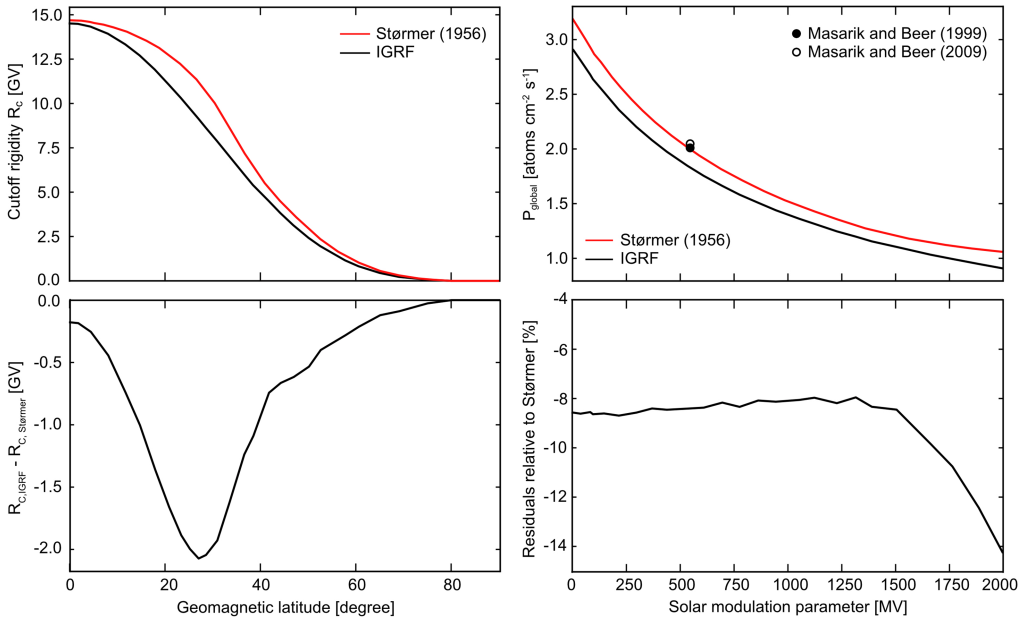


Figure 12. Left-hand panels: cutoff rigidity values as a function of geomagnetic latitude derived with the Størmer's equation (i.e. equation (2.5), in red) and the IGRF [46] (in black) (upper panel) and the corresponding difference between the IGRF and Størmer values (lower panel). Right-hand panels: corresponding global ^{10}Be production rate values in comparison with the model results by Masarik & Beer [59,73] for $\phi = 550$ MV (upper panel) and the corresponding residuals relative to the Størmer's equation (lower panel).

only minor changes in the reproduction rate values are to be expected. In fact, the corresponding global production rate values differ only within 1% from the previous computations. As these changes are negligible, the results are not shown here.

The atmospheric interaction cross-sections are the most crucial of the investigated uncertainties and can result in production rate differences of up to 25% in the case of the cosmogenic radionuclide ^{10}Be.

(c) Dependence on the geomagnetic field models

As shown in §2b, geomagnetic field changes can occur on minute-to-hourly (i.e. externally driven) as well as annual-to-decadal (i.e. internally driven) time scales. Such changes influence the cosmogenic radionuclide production rates. Previous attempts to model the cosmogenic radionuclide production rates often used the analytically derived cutoff rigidity values based on Størmer's equation (i.e. equation (2.6)). As the numeric computations strongly depend on the applied magnetic field model, and particularly on the resulting cutoff rigidities, differences in the resulting production rate calculations are to be expected. The differences in the latitude-dependent cutoff rigidity values based on Størmer's equation (i.e. equation (2.5)) and the IGRF model [46] are shown in the left-hand panels of figure 12. As can be seen, good agreement is only present at high geomagnetic latitudes (i.e. above 70°), while at lower geomagnetic latitudes (i.e. between 24° and 32°) differences of up to –2 GV occur. As Størmer's equation was the foundation of the model efforts by Masarik & Beer [59,73], the upper right-hand panel shows a good example of the corresponding global ^{14}C production rates as a function of the solar modulation parameter based on the LIS model by Garcia-Munoz [23] and the cross-sections by Masarik & Beer [59]. The values derived by Masarik & Beer [59,73] are given by the symbols. As shown in the lower panel, the ^{14}C model efforts based on the IGRF result in production rates that are between 8 to 14% lower than those

Downloaded from royalsocietypublishing.org/rsta/article-pdf/doi/10.1098/rsta.2025.0348/6165301/rsta.2025.0348.pdf
by guest
on 14 September 2026

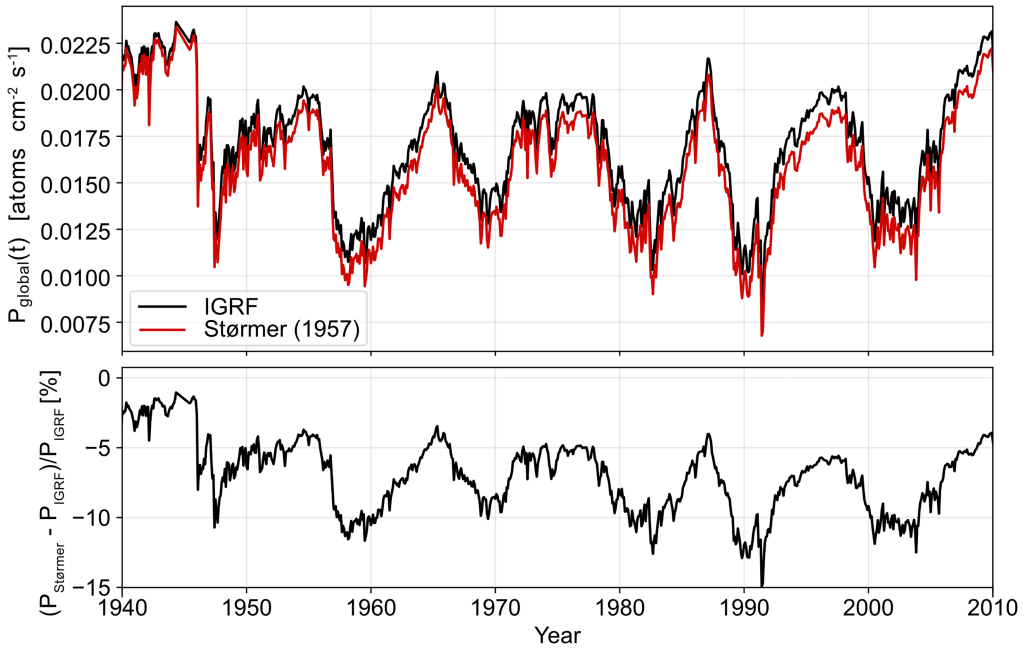


Figure 13. Temporal evolution of the global ^{10}Be production rates based on the IGRF (black) and the Størmer's equation (red).

using the Størmer's equation. To investigate the impact on the temporal ^{10}Be changes, figure 13 shows the corresponding production rates between 1939 and 2010 (same colouring).

It shows that the differences become stronger from the 1940s to the 2000s. Thereby, the relative differences between the two numerically derived production rate values vary between approximately 1% (i.e. 1940s) and up to 15% (i.e. 1990s). Note that hemispheric differences in the ^{10}Be production can be resolved using IGRF-based cutoff rigidities, which cannot be achieved with the Størmer approximation. Zheng *et al.* [84] showed that these differences can reach up to 50% regionally. They further showed that atmospheric transport and deposition processes can reduce the differences to less than 10% and to less than 3% in polar regions. Nevertheless, this conclusion does not imply that the spatial cutoff rigidity pattern can be ignored for ^{10}Be deposition in polar regions, as it may have varied significantly in the past. Further information on the impact of palaeomagnetic field reconstructions on the modelled production is given in Herbst *et al.* [85].

For comparison with Masarik & Beer [73], the proton and alpha LIS models by Garcia-Munoz et al. [23] and the Størmer's equation (equation (2.6)) is used. We further show the ^{14}C results based on the IGRF model (equation (2.7)). Using the IGRF results in 8–14% lower production rate values. Slightly higher differences of 5–15% are reported for ^{10}Be.

4. Summary and conclusions

Several model efforts describing the production of cosmogenic radionuclides have been documented in the literature. However, a systematic discussion of the results within the context of numerically induced changes has been lacking thus far. Initially, we explored the dependencies of the production rates of ^{10}Be, ^{14}C and ^{36}Cl on the local interstellar medium, demonstrating that the maxima of the radionuclide-dependent production response functions shift towards higher energies as solar activity increases. As ^{36}Cl is the radionuclide most sensitive to changes in the

Downloaded from royalsocietypublishing.org/rsta/article-pdf/doi/10.1098/rsta.2025.0348/6165301/rsta.2025.0348.pdf
by guest
on 14 September 2026

Table 2. Systematic error budget for cosmogenic radionuclide production modelling.

model component	source of systematic error	uncertainty (absolute values)	impact on long-term/relative trends
LIS	choice of LIS spectrum	depending on the used LIS model up to **15%** during phases of high solar activity and up to **20–30%** during low solar activity	**significant**, however, if the underlying modulation parameters are properly converted for each LIS model the impact is negligible
nuclear cross-sections	discrepancies in available cross-section datasets	**20–30%** for ^{10}Be	**significant**, one of the primary sources of uncertainty in modelled absolute production rates
geomagnetic field	semi-analytic versus observation-based approximation	production rate differences of up to **50%** for regional production rates and up to **14%** for global production rates	**significant**, particularly for relative variations
atmospheric yield	differences in (i) the numerical particle interaction models and (ii) by applying a weighting factor to account for the geometrical factor	(i) $>$**10%** at low solar activity ($\phi < 500$ MV) (ii) $<$**5%** for secondary particle production at Earth [79]	**modest**, generally negligible, particularly during high solar activity

lower-energy ranges, its response function peak is shifted to lower energies during solar minimum periods, while during high solar activity phases the values are comparable with ^{10}Be and ^{14}C. Using different LIS models, we further demonstrated that the response functions are LIS-model dependent and show LIS-dependent sensitivity to solar activity changes (figure 7). The latter has sufficient consequences for the absolute global production rate values, as variations from 20% (^{10}Be) to 30% (^{36}Cl) occur for low solar activity phases, whereas variations up to 15% occur for high solar activity phases (figure 10). However, as discussed in Herbst *et al.* [11,12], this comparison omits the dependence of the solar modulation parameter on the LIS, and LIS-dependent solar modulation parameter conversions have to be applied. It shows that, based on this correction, the corresponding relative changes are almost negligible for all three cosmogenic radionuclides. Thus, reconstructing solar activity from cosmogenic radionuclide records is more reliable when relative production rate calculations are used [80].

Further, we investigated the influence of cross-sections available in the literature on cosmogenic radionuclide production. Of particular interest are ^{10}Be and ^{14}C, as recent updates have been proposed. As previously discussed in Herbst [13] and Matthiä *et al.* [57], our investigations suggest that modelled global production rates are significantly influenced by the use of different cross-sections. Thereby, differences of more than 25% (20%) occur during low (high) solar activity phases when the production rates based on the cross-sections by Masarik & Beer [59] and Webber & Higbie [24] are compared. However, applying the latest ^{16}O(n,x)^{10}Be cross-section updates by Chen *et al.* [82] reveals that recent model efforts based on the cross-sections by Webber & Higbie [24] are underestimated by 30% (figure 11).

We also investigated the influence of geomagnetic field models on the global production rates. Therefore, we compared the cutoff rigidity values based on the semi-analytic approach by Størmer [44] to the ones derived based on the IGRF [46]. The corresponding absolute production rate values

Downloaded from royalsocietypublishing.org/rsta/article-pdf/doi/10.1098/rsta.2025.0348/6165301/rsta.2025.0348.pdf
by guest
on 14 September 2026

showed a difference of up to 20% (figure 12). While the long-term trend of 1939 to 2010 suggests that the relative differences are only within 5% (figure 13).

Overall, our results suggest that the most critical factors for cosmogenic radionuclide production modelling are (i) the choice of LIS model and (ii) the adopted nuclear cross-sections, especially for ^{10}Be. While raw LIS-dependent production rates can differ by up to 20–30%, these differences become almost negligible once the modulation parameters are properly converted, making relative production rates a robust basis for solar activity reconstructions. By contrast, variations in nuclear cross-sections can lead to persistent discrepancies of 20–30% in absolute production, underscoring the need for up-to-date cross-section data such as the revised ^{16}O(n,x)^{10}Be measurements. The choice of geomagnetic field model affects absolute production at levels less than or equal to 20% and impacts long-term trends within 5%. However, for relative variations, the choice and inclusion of the geomagnetic model is a major uncertainty. A summary of our results is listed in table 2.

A critical challenge in resolving solar activity back in time is the 'observation gap' between instrumental and radionuclide-based records of SEP events, which is fundamentally complicated by the fact that systematic model adjustments do not affect these two populations equally. While, for example, geomagnetic shielding is precisely defined for the instrumental era, historical radionuclide reconstructions rely on underconstrained dipole moment models (e.g. VADM), where regional data biases can introduce significant systematic errors. Furthermore, detecting smaller radionuclide SEP events requires distinguishing their signal from the GCR-induced production background, a task heavily dependent on the chosen LIS and its modulation. Because SEP events typically exhibit soft spectra with higher intensities at lower energies compared to the harder GCR spectra, the resulting atmospheric radionuclide production response—the product of the particle spectrum and the yield function—weights updates in nuclear cross-sections and atmospheric yield functions differently. For instance, a revision in ^{10}Be cross-sections or a shift to a more realistic LIS fixed to Voyager data will shift GCR- and SEP-dependent production rates nonlinearly, potentially widening or narrowing the perceived observation gap. Consequently, investigating these disparate energy-dependent responses is essential to determine whether this gap reflects physical solar variability or is an artefact of the nonlinear scaling inherent in current numerical modelling. Last but not least, it remains uncertain whether the enormous palaeoevents can be regarded merely as scaled-up versions of the known events from the instrumental era or if different processes (e.g. multi-CME passage) must be considered to obtain realistic fluence estimates.

In addition, other factors—such as galactic variability associated with passages through spiral arms, heliospheric variability and changes or reversals of the geomagnetic field—require further investigation. While the LISM and geomagnetic field appear to have been relatively stable over the past approximately 10 000 years (i.e. during the Holocene), the solar system has, on longer time scales, passed through denser and cooler interstellar regions. Zucker *et al*. [86] found that a series of 14 to 20 supernovae responsible for carving out the Local Bubble over the last 10–15 million years has polluted the Sun's environment with nucleosynthetic products. Evidence of such encounters comes from detections of ^{60}Fe, a radioactive isotope produced primarily in supernova explosions, in deep sea crusts [87,88]. Recently, Koll *et al.* [89] also reported a ^{10}Be anomaly (with a 25% increase with respect to the baseline at younger ages) in deep-ocean ferromanganese crusts during the Late Miocene (i.e. around 9–11.5 Myr ago). Together, these three findings are indicative of a much higher GCR flux at Earth during these particular periods. In a first study, Herbst [13] investigated the influence of galactic and heliospheric variations on the ^{10}Be production. Using the GCR spectra for a galaxy arm passage provided by Büsching *et al.* [6], Herbst [13] reported up to 20% higher ^{10}Be production rate values than that of today. In addition, being surrounded by a perturbed low-density interstellar medium with an inflow speed of 100 km s^{-1} resulting in a drastically smaller heliosphere with a termination shock at 11 AU [90] would result in up to 15% higher ^{10}Be production rate values.

Downloaded from royalsocietypublishing.org/rsta/article-pdf/doi/10.1098/rsta.2025.0348/6165301/rsta.2025.0348.pdf
by guest
on 14 September 2026

Data accessibility. This article has no additional data.

Supplementary material is available online [91].

Declaration of AI use. QuillBot (http://www.quillbot.com/) has been used for grammar checking.

Authors' contributions. K.H.: conceptualization, data curation, investigation, methodology, validation, visualization, writing—original draft, writing—review and editing; S.D.: conceptualization, writing—original draft, writing—review and editing; N.E.E.: conceptualization, writing—original draft, writing—review and editing; R.M.: conceptualization, writing—original draft, writing—review and editing; M.O.: conceptualization, visualization, writing—original draft, writing—review and editing; M.Z.: conceptualization, writing—original draft, writing—review and editing.

All authors gave final approval for publication and agreed to be held accountable for the work performed therein.

Conflict of interest declaration. We declare we have no competing interests.

Funding. K.H. acknowledges support from the Research Council of Norway through the Centres of Excellence funding scheme, project number 332523 (PHAB). S.D. acknowledges support from the UK Science and Technology Facilities Council (STFC) through grant no. ST/Y002725/1. This project further has received funding from the European Union (ERC, PastSolarStorms, 10114267 to R.M.). M.O. is part-funded by STFC grant no. UKRI1207 and Natural Environment Research Council (NERC) grant no. NE/Y001052/1. M.Z. acknowledges support from National Natural Science Foundation of China (grant no. 2502173).

Acknowledgements. Views and opinions expressed are those of the author(s) only and do not necessarily reflect those of the European Union or the European Research Council. Neither the European Union nor the granting authority can be held responsible for them.

References

1. Grosse AV. 1934 An unknown radioactivity. *J. Am. Chem. Soc.* **56**, 1922–1924. (doi:10.1021/ja01324a503)
2. Libby WF. 1946 Atmospheric helium three and radiocarbon from cosmic radiation. *Phys. Rev.* **69**, 671–672. (doi:10.1103/PhysRev.69.671.2)
3. Libby WF, Anderson EC, Arnold JR. 1949 Age determination by radiocarbon content: world-wide assay of natural radiocarbon. *Science* **109**, 227–228. (doi:10.1126/science.109.2827.227)
4. Muller RA. 1977 Radioisotope dating with a cyclotron. *Science* **196**, 489–494. (doi:10.1126/science.196.4289.489)
5. Beer J, McCracken K, von Steiger R. 2012 *Cosmogenic radionuclides: theory and applications in the terrestrial and space environments*. Berlin, Germany: Springer.
6. Büsching I, Kopp A, Pohl M, Schlickeiser R, Perrot C, Grenier I. 2005 Cosmic-ray propagation properties for an origin in supernova remnants. *Astrophys. J.* **619**, 314–326. (doi:10.1086/426537)
7. Simpson JA. 2000 The cosmic ray nucleonic component: the invention and scientific uses of the neutron monitor – (keynote lecture). *Space Sci. Rev.* **93**, 11–32. (doi:10.1023/A:1026567706183)
8. Miyake F, Nagaya K, Masuda K, Nakamura T. 2012 A signature of cosmic-ray increase in AD 774–775 from tree rings in Japan. *Nature* **486**, 240–242. (doi:10.1038/nature11123)
9. Miyake F, Masuda K, Hakozaki M, Nakamura T, Tokanai F, Kato K, Kimura K, Mitsutani T. 2014 Verification of the cosmic-ray event in AD 993–994 by using a Japanese hinoki tree. *Radiocarbon* **56**, 1189–1194. (doi:10.2458/56.17769)
10. Mekhaldi F *et al*. 2015 Multiradionuclide evidence for the solar origin of the cosmic-ray events of AD 774/5 and 993/4. *Nat. Commun.* **6**, 8611. (doi:10.1038/ncomms9611)
11. Herbst K, Kopp A, Heber B, Steinhilber F, Fichtner H, Scherer K, Matthiä D. 2010 On the importance of the local interstellar spectrum for the solar modulation parameter. *J. Geophys. Res. Atmos.* **115**, D00I20. (doi:10.1029/2009JD012557)
12. Herbst K, Muscheler R, Heber B. 2017 The new local interstellar spectra and their influence on the production rates of the cosmogenic radionuclides ^{10}Be and ^{14}C. *J. Geophys. Res. Space Phys.* **122**, 23–34. (doi:10.1002/2016JA023207)
13. Herbst K. 2013 Interaction of cosmic rays with the Earth's magnetosphere and atmosphere: modeling the cosmic ray induced ionization and the production of cosmogenic radionuclides. PhD thesis, Christian-Albrechts-Universität zu Kiel, Germany.

Downloaded from royalsocietypublishing.org/rsta/article-pdf/doi/10.1098/rsta.2025.0348/6165301/rsta.2025.0348.pdf
by guest
on 14 September 2026

14. Stone EC, Cummings AC, McDonald FB, Heikkila BC, Lal N, Webber WR. 2013 Voyager 1 observes low-energy galactic cosmic rays in a region depleted of heliospheric ions. *Science* **341**, 150–153. (doi:10.1126/science.1236408)
15. Webber WR, McDonald FB. 2013 Recent Voyager 1 data indicate that on 25 August 2012 at a distance of 121.7 AU from the Sun, sudden and unprecedented intensity changes were observed in anomalous and galactic cosmic rays. *Geophys. Res. Lett.* **40**, 1665–1668. (doi:10.1002/grl.50383)
16. Rankin JS, Stone EC, Cummings AC, McComas DJ, Lal N, Heikkila BC. 2019 Galactic cosmic-ray anisotropies: *Voyager* 1 in the local interstellar medium. *Astrophys. J.* **873**, 46. (doi:10.3847/1538-4357/ab041f)
17. Florinski V *et al*. 2024 Magnetic trapping of galactic cosmic rays in the outer heliosheath and their preferential entry into the heliosphere. *Astrophys. J.* **961**, 244. (doi:10.3847/1538-4357/ad0b15)
18. Adriani O *et al*. 2013 Measurement of the isotopic composition of hydrogen and helium nuclei in cosmic rays with the PAMELA experiment. *Astrophys. J.* **770**, 2. (doi:10.1088/0004-637X/770/1/2)
19. Aguilar M *et al*. 2015 Precision measurement of the proton flux in primary cosmic rays from rigidity 1 GV to 1.8 TV with the alpha magnetic spectrometer on the International Space Station. *Phys. Rev. Lett.* **114**, 171103. (doi:10.1103/PhysRevLett.114.171103)
20. Potgieter MS, Vos EE, Boezio M, De Simone N, Di Felice V, Formato V. 2014 Modulation of galactic protons in the heliosphere during the unusual solar minimum of 2006 to 2009. *Sol. Phys.* **289**, 391–406. (doi:10.1007/s11207-013-0324-6)
21. Bisschoff D, Potgieter MS. 2016 New local interstellar spectra for protons, helium and carbon derived from PAMELA and Voyager 1 observations. *Astrophys. Space Sci.* **361**, 48. (doi:10.1007/s10509-015-2633-8)
22. Corti C, Bindi V, Consolandi C, Whitman K. 2016 Solar modulation of the local interstellar spectrum with Voyager 1, AMS-02, PAMELA, and BESS. *Astrophys. J.* **829**, 8. (doi:10.3847/0004-637x/829/1/8)
23. Garcia-Munoz M, Mason GM, Simpson JA. 1975 The anomalous ^{4}He component in the cosmic-ray spectrum at $\lessapprox 50$ MeV per nucleon during 12972 - 1974. *Astrophys. J.* **202**, 265–275. (doi:10.1086/153973)
24. Webber WR, Higbie PR. 2003 Production of cosmogenic Be nuclei in the Earth's atmosphere by cosmic rays: its dependence on solar modulation and the interstellar cosmic ray spectrum. *J. Geophys. Res. Space Phys.* **108**, 1355. (doi:10.1029/2003JA009863)
25. Usoskin IG, Alanko-Huotari K, Kovaltsov GA, Mursula K. 2005 Heliospheric modulation of cosmic rays: monthly reconstruction for 1951–2004. *J. Geophys. Res. Space Phys.* **110**, A12108. (doi:10.1029/2005JA011250)
26. Parker EN. 1965 The passage of energetic charged particles through interplanetary space. *Planet. Space Sci.* **13**, 9–49. (doi:10.1016/0032-0633(65)90131-5)
27. Burger RA, Krüger TPJ, Hitge M, Engelbrecht NE. 2008 A Fisk–Parker hybrid heliospheric magnetic field with a solar-cycle dependence. *Astrophys. J.* **674**, 511–519. (doi:10.1086/525039)
28. Engelbrecht NE, Effenberger F, Florinski V, Potgieter MS, Ruffolo D, Chhiber R, Usmanov AV, Rankin J, Els PL. 2022 Theory of cosmic ray transport in the heliosphere. *Space Sci. Rev.* **218**, 33. (doi:10.1007/s11214-022-00896-1)
29. Gleeson LJ, Axford WI. 1968 Solar modulation of galactic cosmic rays. *Astrophys. J.* **154**, 1011. (doi:10.1086/149822)
30. Caballero-Lopez RA, Moraal H. 2004 Limitations of the force field equation to describe cosmic ray modulation. *J. Geophys. Res. Space Phys.* **109**, A01101. (doi:10.1029/2003JA010098)
31. Moraal H. 2013 Cosmic-ray modulation equations. *Space Sci. Rev.* **176**, 299–319. (doi:10.1007/s11214-011-9819-3)
32. Engelbrecht NE, Di Felice V. 2020 Uncertainties implicit to the use of the force-field solutions to the Parker transport equation in analyses of observed cosmic ray antiproton intensities. *Phys. Rev. D* **102**, 103007. (doi:10.1103/PhysRevD.102.103007)
33. Compton AH, Getting IA. 1935 An apparent effect of galactic rotation on the intensity of cosmic rays. *Phys. Rev.* **47**, 817–821. (doi:10.1103/PhysRev.47.817)
34. Gleeson LJ, Axford WI. 1968 The compton-getting effect. *Astrophys. Space Sci.* **2**, 431–437. (doi:10.1007/BF02175919)

Downloaded from royalsocietypublishing.org/rsta/article-pdf/doi/10.1098/rsta.2025.0348/6165301/rsta.2025.0348.pdf
by guest
on 14 September 2026

35. Usoskin IG, Bazilevskaya GA, Kovaltsov GA. 2011 Solar modulation parameter for cosmic rays since 1936 reconstructed from ground-based neutron monitors and ionization chambers. *J. Geophys. Res. Space Phys.* **116**, A02104. (doi:10.1029/2010JA016105)
36. Gieseler J, Heber B, Herbst K. 2017 An empirical modification of the force field approach to describe the modulation of galactic cosmic rays close to Earth in a broad range of rigidities. *J. Geophys. Res. Space Phys.* **122**, 10 964–10 979. (doi:10.1002/2017JA024763)
37. Jokipii JR, Levy EH, Hubbard WB. 1977 Effects of particle drift on cosmic-ray transport. I. General properties, application to solar modulation. *Astrophys. J. Lett.* **213**, 861–868. (doi:10.1086/155218)
38. Mohlolo ST, Engelbrecht NE, Ferreira SES. 2022 A detailed comparison of techniques used to model drift in numerical cosmic ray modulation models. *Adv. Space Res.* **69**, 2574–2588. (doi:10.1016/j.asr.2021.12.035)
39. Shalchi A. 2009 *Nonlinear cosmic ray diffusion theories*, vol. 362. Berlin, Germany: Springer.
40. Els PL, Engelbrecht NE, Lang JT, Strauss RD. 2024 The diffusion tensor of protons at 1 au: comparing simulation, observation, and theory. *Astrophys. J.* **975**, 134. (doi:10.3847/1538-4357/ad7c44)
41. Lang JT, Strauss RD, Engelbrecht NE, van den Berg JP, Dresing N, Ruffolo D, Bandyopadhyay R. 2024 A detailed survey of the parallel mean free path of solar energetic particle protons and electrons. *Astrophys. J.* **971**, 105. (doi:10.3847/1538-4357/ad55c3)
42. Kóta J. 2013 Theory and modeling of galactic cosmic rays: trends and prospects. *Space Sci. Rev.* **176**, 391–403. (doi:10.1007/s11214-012-9870-8)
43. Potgieter MS. 2013 Solar modulation of cosmic rays. *Living Rev. Sol. Phys.* **10**, 3. (doi:10.12942/lrsp-2013-3)
44. Størmer C. 1956 The polar aurora. *Q. J. R. Meteorol. Soc.* **82**, 115. (doi:10.1002/qj.49708235123)
45. Pilchowski J, Kopp A, Herbst K, Heber B. 2010 On the definition and calculation of a generalised McIlwain parameter. *Astrophys. Space Sci. Trans.* **6**, 9–17. (doi:10.5194/astra-6-9-2010)
46. Alken P *et al*. 2021 International geomagnetic reference field: the thirteenth generation. *Earth Planets Space* **73**, 49. (doi:10.1186/s40623-020-01288-x)
47. Korte M, Muscheler R. 2012 Centennial to millennial geomagnetic field variations. *J. Space Weather Space Clim.* **2**, A08. (doi:10.1051/swsc/2012006)
48. Snowball I, Muscheler R. 2007 Palaeomagnetic intensity data: an Achilles heel of solar activity reconstructions. *Holocene* **17**, 851–859. (doi:10.1177/0959683607080531)
49. Panovska S, Korte M, Finlay CC, Constable CG. 2015 Limitations in paleomagnetic data and modelling techniques and their impact on Holocene geomagnetic field models. *Geophys. J. Int.* **202**, 402–418. (doi:10.1093/gji/ggv137)
50. Yang S, Odah H, Shaw J. 2000 Variations in the geomagnetic dipole moment over the last 12 000 years. *Geophys. J. Int.* **140**, 158–162. (doi:10.1046/j.1365-246X.2000.00011.x)
51. Korte M, Constable C, Donadini F, Holme R. 2011 Reconstructing the Holocene geomagnetic field. *Earth Planet. Sci. Lett.* **312**, 497–505. (doi:10.1016/j.epsl.2011.10.031)
52. Licht A, Hulot G, Gallet Y, Thébault E. 2013 Ensembles of low degree archeomagnetic field models for the past three millennia. *Phys. Earth Planet. Inter.* **224**, 38–67. (doi:10.1016/j.pepi.2013.08.007)
53. Knudsen MF, Riisager P, Donadini F, Snowball I, Muscheler R, Korhonen K, Pesonen LJ. 2008 Variations in the geomagnetic dipole moment during the Holocene and the past 50 kyr. *Earth Planet. Sci. Lett.* **272**, 319–329. (doi:10.1016/j.epsl.2008.04.048)
54. Nilsson A, Holme R, Korte M, Suttie N, Hill M. 2014 Reconstructing Holocene geomagnetic field variation: new methods, models and implications. *Geophys. J. Int.* **198**, 229–248. (doi:10.1093/gji/ggu120)
55. Nilsson A, Nguyen L, Panovska S, Herbst K, Zheng M, Suttie N, Muscheler R. 2024 Holocene solar activity inferred from global and hemispherical cosmic-ray proxy records. *Nat. Geosci.* **17**, 654–659. (doi:10.1038/s41561-024-01467-5)
56. Herbst K, Kopp A, Heber B. 2013 Influence of the terrestrial magnetic field geometry on the cutoff rigidity of cosmic ray particles. *Ann. Geophys.* **31**, 1637–1643. (doi:10.5194/angeo-31-1637-2013)
57. Matthiä D, Herbst K, Heber B, Berger T, Reitz G. 2013 ^{10}Be production in the atmosphere by galactic cosmic rays. *Space Sci. Rev.* **176**, 333–342. (doi:10.1007/s11214-011-9817-5)

Downloaded from royalsocietypublishing.org/rsta/article-pdf/doi/10.1098/rsta.2025.0348/6165301/rsta.2025.0348.pdf
by guest
on 14 September 2026

58. Herbst K. 2016 Modelling the production of cosmogenic radionuclides due to galactic and solar cosmic rays. In *34th Int. Cosmic Ray Conf. (ICRC2015)*, vol. 236, p. 537. Trieste, Italy: SISSA Medialab srl. (doi:10.22323/1.236.0537)
59. Masarik J, Beer J. 1999 Simulation of particle fluxes and cosmogenic nuclide production in the Earth's atmosphere. *J. Geophys. Res. Atmos.* **104**, 12 099–12 111. (doi:10.1029/1998JD200091)
60. Michel R. 2007 Cross sections for the production of residual nuclides at medium energies: status and recent experimental and theoretical progress. *AIP Conf. Proc.* **891**, 237–245. (doi:10.1063/1.2713523)
61. Reedy RC. 2013 Cosmogenic-nuclide production rates: reaction cross section update. *Nucl. Instrum. Methods Phys. Res. B Beam Interact. Mater. At.* **294**, 470–474. (doi:10.1016/j.nimb.2011.08.034)
62. Beer J, McCracken K, von Steiger R. 2012 *Cosmogenic radionuclides: theory and applications in the terrestrial and space environments*. Berlin, Germany: Springer Science & Business Media.
63. Agostinelli S *et al*. 2003 Geant4—a simulation toolkit. *Nucl. Instrum. Methods Phys. Res. A.* **506**, 250–303. (doi:10.1016/S0168-9002(03)01368-8)
64. Desorgher L, Flückiger E, Gurtner M. 2006 The PLANETOCOSMICS Geant4 application. In *36th COSPAR Sci. Assembly*, vol. 36, p. 2361. Paris, France: COSPAR.
65. Poluianov SV, Kovaltsov GA, Mishev AL, Usoskin IG. 2016 Production of cosmogenic isotopes ^{7}Be, ^{10}Be, ^{14}C, ^{22}Na, and ^{36}Cl in the atmosphere: altitudinal profiles of yield functions. *J. Geophys. Res. Atmos.* **121**, 8125–8136. (doi:10.1002/2016JD025034)
66. Clem JM, Dorman LI. 2000 Neutron monitor response functions. *Space Sci. Rev.* **93**, 335–359. (doi:10.1023/A:1026508915269)
67. Koi T, Asai M, Wright D, Niita K, Nara Y, Amako K, Sasaki T. 2003 Interfacing the JQMD and JAM nuclear reaction codes to Geant4. In *Comput. High Energy Nucl. Phys.*, pp. 24–28. La Jolla, CA: SLAC National Accelerator Laboratory.
68. Adolphi F, Herbst K, Nilsson A, Panovska S. 2023 On the polar bias in ice core ^{10}Be data. *J. Geophys. Res. Atmos.* **128**, e2022JD038203. (doi:10.1029/2022JD038203)
69. Zheng M, Adolphi F, Ferrachat S, Mekhaldi F, Lu Z, Nilsson A, Lohmann U. 2024 Modeling atmospheric transport of cosmogenic radionuclide ^{10}Be using GEOS-Chem 14.1.1 and ECHAM6.3-HAM2.3: implications for solar and geomagnetic reconstructions. *Geophys. Res. Lett.* **51**, e2023GL106642. (doi:10.1029/2023GL106642)
70. Lal D, Peters B. 1967 Cosmic ray produced radioactivity on the earth. In *Kosmische Strahlung II / Cosmic Rays II* (ed. K Sitte), pp. 551–612. Berlin, Germany: Springer.
71. Damon PE, Lerman JC, Long A. 1978 Temporal fluctuations of atmospheric ^{14}C: causal factors and implications. *Annu. Rev. Earth Planet. Sci.* **6**, 457–494. (doi:10.1146/annurev.ea.06.050178.002325)
72. Masarik J, Reedy RC. 1995 Terrestrial cosmogenic-nuclide production systematics calculated from numerical simulations. *Earth Planet. Sci. Lett.* **136**, 381–395. (doi:10.1016/0012-821X(95)00169-D)
73. Masarik J, Beer J. 2009 An updated simulation of particle fluxes and cosmogenic nuclide production in the Earth's atmosphere. *J. Geophys. Res. Atmos.* **114**, D11103. (doi:10.1029/2008JD010557)
74. Kovaltsov GA, Mishev A, Usoskin IG. 2012 A new model of cosmogenic production of radiocarbon ^{14}C in the atmosphere. *Earth Planet. Sci. Lett.* **337–338**, 114–120. (doi:10.1016/j.epsl.2012.05.036)
75. Reyss J-L, Yokoyama Y, Guichard F. 1981 Production cross sections of ^{26}Al, ^{22}Na, ^{7}Be from argon and of ^{10}Be, ^{7}Be from nitrogen: implications for production rates of ^{26}Al and ^{10}Be in the atmosphere. *Earth Planet. Sci. Lett.* **53**, 203–210. (doi:10.1016/0012-821X(81)90154-0)
76. Lange H-J *et al*. 1995 Production of residual nuclei by α-induced reactions on C, N, O, Mg, Al and Si up to 170 MeV. *Appl. Radiat. Isot.* **46**, 93–112. (doi:10.1016/0969-8043(94)00124-I)
77. Jull AJT, Cloudt S, Donahue DJ, Sisterson JM, Reedy RC, Masarik J. 1998 ^{14}C depth profiles in Apollo 15 and 17 cores and lunar rock 68815. *Geochim. Cosmochim. Acta* **62**, 3025–3036. (doi:10.1016/S0016-7037(98)00193-8)
78. Tatischeff V, Kozlovsky B, Kiener J, Murphy RJ. 2006 Delayed X- and gamma-ray line emission from solar flare radioactivity. *Astrophys. J. Suppl. Ser.* **165**, 606–617. (doi:10.1086/505112)

Downloaded from royalsocietypublishing.org/rsta/article-pdf/doi/10.1098/rsta.2025.0348/6165301/rsta.2025.0348.pdf
by guest
on 14 September 2026

79. Matthiä D. 2009 The radiation environment in the lower atmosphere: a numerical approach. PhD thesis, Christian-Albrechts-Universität zu Kiel, Germany.
80. Muscheler R, Adolphi F, Herbst K, Nilsson A. 2016 The revised sunspot record in comparison to cosmogenic radionuclide-based solar activity reconstructions. *Sol. Phys.* **291**, 3025–3043. (doi:10.1007/s11207-016-0969-z)
81. Caffee MW, Nishiizumi K, Sisterson JM, Ullmann J, Welten KC. 2013 Cross section measurements at neutron energies 71 and 112 MeV and energy integrated cross section measurements ($0.1 < E_n < 750$ MeV) for the neutron induced reactions O(n,x)^{10}Be, Si(n,x)^{10}Be, and Si(n,x)^{26}Al. *Nucl. Instrum. Methods Phys. Res. B* **294**, 479–483. (doi:10.1016/j.nimb.2012.07.011)
82. Chen J, Dong T, Ren Z. 2016 Cross sections of proton- and neutron-induced reactions by the Liège intranuclear cascade model. *Phys. Rev. C* **93**, 064608. (doi:10.1103/PhysRevC.93.064608)
83. Wallner A *et al*. 2016 Accelerator mass spectrometry measurements of the $^{13}C(n,\gamma)^{14}C$ and $^{14}N(n,p)^{14}C$ cross sections. *Phys. Rev. C* **93**, 045803. (doi:10.1103/PhysRevC.93.045803)
84. Zheng M, Liu H, Adolphi F, Muscheler R, Lu Z, Wu M, Prisle NL. 2023 Simulations of ^{7}Be and ^{10}Be with the GEOS-Chem global model v14.0.2 using state-of-the-art production rates. *Geosci. Model Dev.* **16**, 7037–7057. (doi:10.5194/gmd-16-7037-2023)
85. Herbst K, Beer J, Heber B, Kopp A. 2013 Self-consistent modeling of cosmogenic radionuclide production rates during the Holocene. In *Proc. 33rd Int. Cosmic Ray Conf.*, vol. 33, p. 2535. Rio de Janeiro, Brazil: Centro Brasileiro de Pesquisas Físicas. https://ui.adsabs.harvard.edu/abs/2013ICRC...33.2535H/abstract.
86. Zucker C, Redfield S, Starecheski S, Konietzka R, Linsky JL. 2025 The origin of the cluster of local interstellar clouds. *Astrophys. J.* **986**, 58. (doi:10.3847/1538-4357/adc920)
87. Feige J, Wallner A, Winkler SR, Merchel S, Fifield LK, Korschinek G, Rugel G, Breitschwerdt D. 2012 The search for supernova-produced radionuclides in terrestrial deep-sea archives. *Publ. Astron. Soc. Aust.* **29**, 109–114. (doi:10.1071/AS11070)
88. Wallner A *et al*. 2021 ^{60}Fe and ^{244}Pu deposited on Earth constrain the r-process yields of recent nearby supernovae. *Science* **372**, 742–745. (doi:10.1126/science.aax3972)
89. Koll D *et al*. 2025 A cosmogenic ^{10}Be anomaly during the late Miocene as independent time marker for marine archives. *Nat. Commun.* **16**, 866. (doi:10.1038/s41467-024-55662-4)
90. Scherer K, Fichtner H, Heber B, Ferreira SES, Potgieter MS. 2008 Cosmic ray flux at the Earth in a variable heliosphere. *Adv. Space Res.* **41**, 1171–1176. (doi:10.1016/j.asr.2007.03.016)
91. Herbst K, Dalla S, Engelbrecht NE, Muscheler R, Owens M, Zheng M. 2026 Supplementary material from: Assessing uncertainties in the numerical modelling of cosmogenic radionuclide production. Figshare. (doi:10.6084/m9.figshare.c.8623422)

Downloaded from royalsocietypublishing.org/rsta/article-pdf/doi/10.1098/rsta.2025.0348/6165301/rsta.2025.0348.pdf
by guest
on 14 September 2026